Wind-Forced Downwelling Slope Currents: A Numerical Study

John F. Middleton and Mauro Cirano

School of Mathematics, University of New South Wales, Sydney, New South Wales, Australia

ABSTRACT

A study is made of the dynamics of slope currents that arise from a steady, constant alongshore wind over a uniform shelf. Over the first 10–20 days, the evolution of the downwelled system on an f plane is qualitatively described by linear coastal-trapped wave dynamics. After this time the thermal wind shear associated with the bottom mixed layer becomes important in the evolution of the undercurrent (UC), which is shown to be driven by the alongshore pressure gradient due to sea level. As the UC over the slope evolves, the bottom Ekman transport becomes small and negative, leading to the detachment of flow near the shelf break, localized spreading of isopycnals, and further intensification of the UC. In contrast to results obtained without bottom drag, bottom friction and boundary layer transport are shown to lead to a two- to threefold increase in cross-shelf interior transport, downwelling, and thermal wind shear. By day 60, the resultant UC has speeds of up to 15 cm s^{-1} and a net transport of 0.7 Sv (Sv $\equiv$ 10^6 m^3 s^{-1}), or ⅔ of the surface Ekman transport. The alongshore transport associated with the UC is shown to be fed and drained by on- and offshore transports of comparable magnitude to the UC. The reduction in bottom stress over the shelf also leads to an alongshore current and density field that change little over many hundreds of kilometers. The sensitivity of results to the stratification, bathymetry, and wind stress curl is outlined and some suggestions are made regarding the shelf circulation forced by winds within the Great Australian Bight.

1. Introduction

During the austral winter, the mean winds within the Great Australian Bight are directed toward the east and drive an onshore Ekman transport that leads to downwelling and an eastward current near the coast. While the shelf circulation in the far west is dominated by the inflow from the Leeuwin Current (Church et al. 1989), wind-forced downwelling may be important over much of the eastern region. Indeed, Lyne and Thresher (1994) present observations that show that the poleward Zeehan Current off the west Tasmanian coast averages speeds of about 50 cm s^{-1} over the winter months. An equatorward undercurrent (UC) is also found (Vince Lyne 1998, personal communication). However, while the bight as a whole extends over more than 3000 km, few current meter observations have been made and the nature of the circulation remains to be determined.

Elsewhere, few investigations have been made into the slope circulation driven by seasonally downwelling favorable winds. The likely reason for this is simply that there are few regions explored to date where both downwelling favorable winds exist and the associated

circulation is dominant. For example, along most eastern ocean boundaries, the winds are generally upwelling favorable (Neshyba et al. 1989), while along the western ocean boundaries, intense currents (driven by basin-scale wind fields) dominate the slope circulation.

One exception appears to be the slope circulation over the Oregon and Washington shelves. Observations show (Hickey 1989) that the alongshelf wind, coastal current (CC), and UC all reverse direction during winter. That is, the CC is poleward and in the direction of the wind, while over the slope an equatorward UC is found. A second example that highlights the importance of downwelling is the Leeuwin Current off the west coast of Australia where a poleward CC and equatorward UC are both found to have speeds of 20 cm s^{-1} or so (Church et al. 1989). The downwelling here is caused by the meridional gradient of density in the Indian Ocean, which, in analogy with wind forcing, drives an onshore flow within the surface mixed layer.

The motivation for this study is to understand the dynamics of wind-forced downwelling with particular regard to the circulation within the Great Australian Bight. As a first step we consider the response to a steady downwelling favorable wind with a finite alongshore fetch. Alongshelf bathymetric variations will not be considered. The problem is quite idealized but we have found no comparable study in the literature. Certainly, the problem of upwelling has received attention.

Corresponding author address: Dr. John F. Middleton, School of Mathematics, University of New South Wales, Sydney 2052, Australia.
E-mail: john.middleton@unsw.edu.au

In an idealized study, McCreary (1981) adopted a vertical coastal wall and using a modal analysis, developed an analytical model for upwelling. A key result was that an alongshore pressure gradient and internal friction were necessary for the existence of a realistic UC. McCreary and Chao (1985) extended these results to obtain steady solutions over a shelf and found that, unlike the flat ocean model, the UC was confined to the region of wind forcing. Within the UC, the cross-shelf flow was found to be downwelling favorable, while above it, an (Ekman) upwelling response was found. The strength of the UC was found to depend upon the following. First, the UC weakened and even disappeared as the depth of the shelf at the coast decreased to realistic values. In this case, the effective strength of the stratification was reduced. Second, on a β plane, Rossby wave propagation was found to leak energy offshore, leading to a strengthening of the UC. Finally, an offshore increase in wind stress was shown to lead to a Sverdrup transport that enhanced the strength of the UC.

These results were complemented by the primitive equation studies of Suginohara (1982) and Suginohara and Kitamura (1984). Suginohara (1982) examined the short-term (0–14 day) evolution of an upwelling favorable current system and found that a weak UC developed below the equatorward CC. The set up of the current system was found to be qualitatively described by the passage of the first two coastal-trapped wave (CTW) modes.

Suginohara and Kitamura (1984) considered the long time (0–160 days) evolution of the current system and for an f plane, found that the weak UC ultimately disappeared. Surprisingly, the inclusion of bottom friction did not lead to any substantial change in the results, suggesting that the bottom boundary layer plays only a minor role in the overall dynamics. Indeed, Suginohara and Kitamura (1984) claimed "the whole stage response is accounted for by CTW dynamics." In accordance with the results of McCreary and Chao (1985), these authors also found that the inclusion of the beta effect led to a strengthening of the UC, although again the magnitude was weak (1.5 cm s^{-1}) compared to the CC (20 cm s^{-1}). The UC was not found to extend far beyond the region of forcing and the marginal intensification of the UC was attributed to the leakage of barotropic energy by westward Rossby wave dispersion.

The above results raise some interesting points within the context of wind-driven downwelling slope currents. First, since the analysis of McCreary and Chao (1985) is based upon linear equations, with a change of sign all of their results are applicable to downwelling current systems. Moreover, since Suginohara and Kitamura (1984) find the long-term f-plane response to be independent of bottom friction and explained by CTW dynamics, we might expect their results to also pertain to downwelling systems. That is, for a realistic shelf geometry with a shallow coastal region, we expect a weak UC to ultimately disappear and the long-term re-

sponse to be independent of bottom friction and qualitatively described by inviscid CTW dynamics. As we will show, none of these expectations will be realized because of the thermal wind shear that arises within the bottom mixed layer.

One-dimensional models have shown that within downwelling boundary layers, the thermal wind shear can be large enough to completely eliminate or "shut down" bottom stress (MacCready and Rhines 1993). In this case we might expect the results here to be independent of bottom friction as Suginohara and Kitamura (1984) found for the upwelling case. However, the shutdown of bottom stress leads to the arrest of the cross-slope Ekman transport. Since the slope and stratification typically vary across a shelf, variations in the Ekman transport can lead to the formation of fronts and profoundly effect the interior flow (Gawarkiewicz and Chapman 1991). Most recently, Chapman and Lentz (1997) have shown that the downstream evolution of an alongshore current may involve a state of complete shutdown so that the slope current may persist indefinitely! None of these studies included wind forcing, although the concepts developed will provide a framework for the analysis of the downwelled circulation.

With the wintertime circulation along the Great Australian Bight in mind, we will examine in detail wind-forced downwelling on an f plane. A summertime stratification will be used for most of the study. There are two reasons for this: First, while wintertime cooling leads to a surface mixed layer 100 m deep within the bight, over the shelf and slope, warm light water is driven eastward over many hundreds of kilometers by the Leeuwin Current. During winter this water and warm, saline water formed at the head of the bight form various tongues and meanders near the edge of the shelf and can be downwelled by 50–100 m (Legeckis and Cresswell 1981; Rochford 1986; Godfrey et al. 1986). Thus, even while the mixed layer is deep offshore, light water over the shelf should act to locally replace the summertime thermocline, which is otherwise found between depths of 25 and 100 m (Levitus and Boyer 1994; Levitus et al. 1994). A second reason for using the "summertime" stratification is simply that the UC is largest in this case and the dynamics of the current system most easily identified.

In section 2, an outline is given of the boundary conditions and configuration of the Princeton Ocean Model (Blumberg and Mellor 1987). In section 3, an overview of the circulation is presented together with an examination of the role of CTWs in determining the initial circulation. The subsequent circulation and UC are examined in section 4 in terms of the dynamics associated with alongshore pressure gradients, friction, and thermal wind shear within the bottom mixed layer. In section 5, we examine the effects that arise from a β-plane, wind stress curl, and variations in bathymetry and stratification. In the summary, some tentative suggestions are
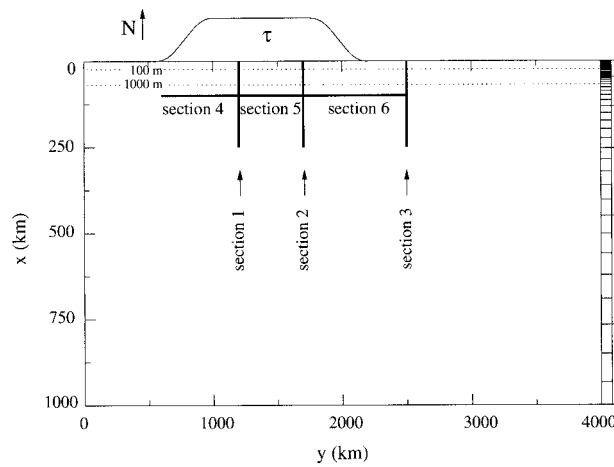
FIG. 1. The model domain including the sections for analysis and the 100-m and 1000-m depth contours (dotted) of the zonal shelf. The direction north (N) and region of wind forcing are indicated above the panel. The seaward ocean has a uniform depth of 1000 m and the cell width in the x direction is indicated on the right edge of the panel.

made regarding the circulation forced by wintertime winds within the Great Australian Bight.

2. Model configuration

The numerical model used is the 1992 version of the Princeton Ocean Model configured for the domain shown in Fig. 1. We take x to be the offshore coordinate and y the alongshore coordinate. The shelf will be taken to extend from west to east as indicated since we are interested in downwelling over zonal shelves.

The shelf depth $h(x)$ is uniform in the alongshore direction and the top 280 m is illustrated in Fig. 2. The shelf intercepts the deep ocean at $(x, h) = (60$ km, 1000 m). As shown along the edge of Fig. 1, the x-grid size varies from about 2 km over the slope to 8 km at the edge of the shelf and then increases linearly by 20% to a maximum of 82 km at the southern end of the ocean basin ($x = 1017$ km). The y-grid size decreases from 40 km at the western end of the domain to 20 km at $y = 500$ km. For $y \in [500, 2500]$ km, the grid size is fixed at 20 km, while farther to the east the grid size increases linearly to 60 km, yielding an alongshore extent of 4000 km. A total of 45 and 145 cells are used in the x and y directions, while in the vertical 40 sigma levels are adopted with greatest resolution near the sur-
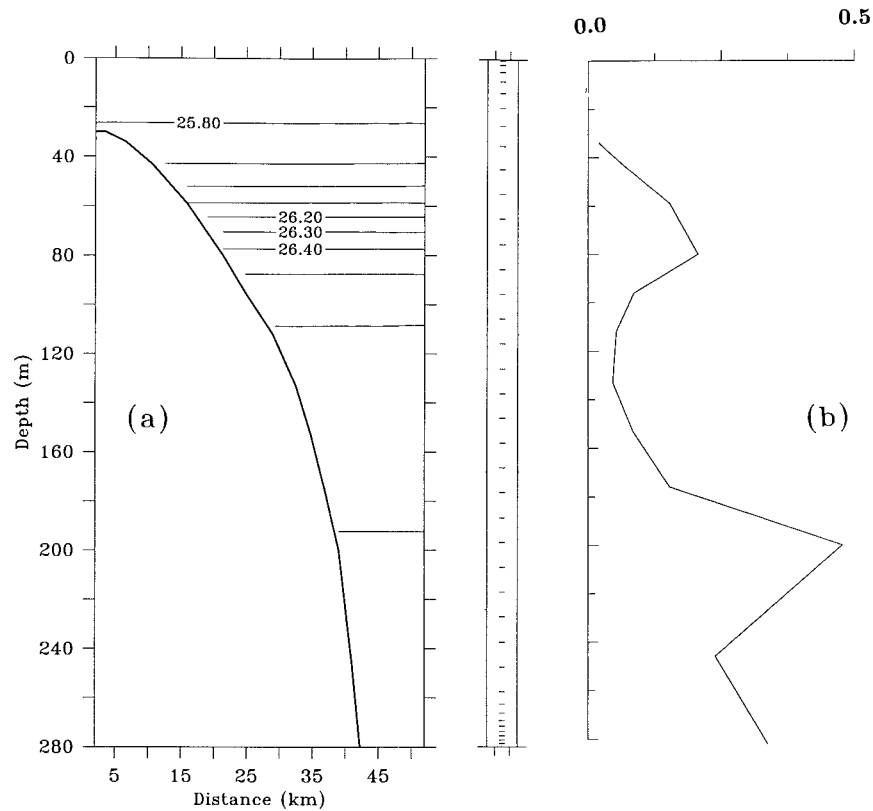

FIG. 2. (a) The shelf bathymetry to a depth of 280 m and the initial density field σ_t. Units kg m^{-3}. (b) The Burger number $S = (Nh_x/f)^2$ based on the initial stratification. The vertical distribution of the 40 sigma cordinates is illustrated by the middle panel.

face and bottom (Fig. 2). To satisfy the CFL criteria (Courant et al. 1967), the internal and external time steps are chosen to be 400 and 10 s, respectively.

The horizontal eddy viscosity (and diffusivity) and the bottom drag coefficient are taken to be 50 m² s⁻¹ and $C_D = 2.5 \times 10^{-3}$, respectively, and a Coriolis parameter for the Southern Hemisphere is chosen as $f = -10^{-4}$ s⁻¹. The vertical diffusivities of momentum, salt, and heat are determined from the Mellor–Yamada turbulence closure scheme and are thus generally zero in the interior where the velocity shear is small. The surface and bottom fluxes of heat and salt are set to zero.

The initial density field (Fig. 2) varies only with depth and is calculated from the summertime (Jan–Mar) seasonal climatology of Levitus et al. (1994) and Levitus and Boyer (1994) and for the South Australian region. From this initial field, the buoyancy frequency N and Burger number $S = (Nh_x/f)^2$ were calculated, and as shown in Fig. 2, the effective stratification indicated by S is largest over the inner and outer shelf and small near the shelf break ($h \approx 140$ m).

The Burger number is important in the context of downwelling favorable flows since the timescale T_S for the shutdown of bottom stress and arrest of the cross-shelf Ekman transport is proportional to $S^{-3/2}$ (Garrett et al. 1993). For the case here (Fig. 2), we might therefore expect the arrest of the bottom mixed layer (BML) transport over the slope to occur before it does near the shelf break. As will be found, the resultant divergence in cross-shelf transport, in turn, leads to the detachment of water from the BML into the interior and enhancement of the thermal wind shear and magnitude of the UC.

The boundary conditions are similar to those adopted by McCreary et al. (1991). No energy should be present at the western boundary since, in the Southern Hemisphere, CTWs can only propagate with the coast on the left. However, model results show that some energy does propagate to the west (along the southern open boundary), so an Orlanski radiation condition was adopted for the western boundary. To absorb any residual energy near the western boundary, a Rayleigh sponge was adopted for sea level η, the depth-averaged velocities (U, V) and the depth-dependent velocities (u, v). For the sponge, the damping coefficient increases linearly from zero at $y = 433$ km, to a value of $1/(2400$ s) at the western boundary ($y = 0$).

A modified Orlanski condition was applied to all variables at the southern open boundary since use of an Orlanski condition led to large numerical instabilities after a few days of model evolution (McCreary et al. 1991). At the eastern boundary, a zero gradient condition was applied so as to allow for the transmission of the wind-driven coastal current.

Forcing of the model was acomplished by an alongshore wind stress tapered in the alongshore direction from zero to a constant value of $\tau^w = 0.1$ Pa between $y = 1000$ km and $y = 1800$ km (Fig. 1). The net surface

Ekman flux is 1.2 Sv (Sv $\equiv 10^6$ m³ s⁻¹), indicating an effective fetch of $L_w = 1200$ km.

The model solutions were found to be subject to weak two-gridpoint instabilities that were most evident in the alongshore direction. Since the alongshore scale of the uncontaminated solutions should exceed the $3\Delta y$ scale of 60 km, the instabilities were kept under reasonable control by applying a Shapiro filter in the alongshore direction and to all time-dependent variables. For sea level the filter may be written as

$$\eta_{i,j} = (1 - \gamma)\eta_{i,j} + 0.5\gamma[\eta_{i,j-1} + \eta_{i,j+1}],$$

where once a model run day, γ, was fixed at 0.5 so as to provide a severe filter. At all other time steps γ was fixed at 0.1.

As a check on artificial pressure gradients that arise from the sigma coordinate system, the model was run for 30 days without any wind forcing. As desired, the velocity field was essentially zero and less than the maximum of 0.5 cm s⁻¹ found over the outer shelf (depth 300 m).

In order to test the influence of the seaward (southern) boundary condition, results were compared with those obtained from a larger domain model. For this model, the domain was doubled in the offshore direction by forming a mirror image of the bathymetry about the $x = 1017$ km axis. The seaward boundary condition is thus replaced by a shelf and coast (at $x = 2034$ km), which serve to trap disturbances that arise there from upwelling. Moreover, to allow for the outflow of the westward CC along this shelf, zero gradient conditions were imposed along $y = 0$ and within 200 km of the new coast. The Rayleigh sponge at the western open boundary was relaxed to zero over $x \in [1400, 1800]$ km and the drag coefficient increased from 2.5×10^{-3} to 2.0×10^{-2} over $x \in [1400, 2034]$ km so as to damp the flow. Computational limitations meant it was necessary to halve the vertical resolution.

In summary, the solutions were found to be almost identical to those presented below using the smaller domain indicating that results are insensitive to both the seaward open boundary condition and vertical resolution. Again, problems associated with artificial pressure gradients do not appear to be significant.

3. An overview and the role of coastal-trapped waves

Here we present an overview of the circulation over 60 model days. In agreement with the upwelling study of Suginohara (1981), the analysis below shows that the initial set up and character of the circulation over the first 10–20 days are qualitatively described by linear, inviscid CTW dynamics. After this time and in contrast to the upwelling case (Suginohara and Kitamura 1984), CTW dynamics do not provide a definitive explanation of the circulation associated with the UC. Rather, the important dynamics here are related to alongshore pres-
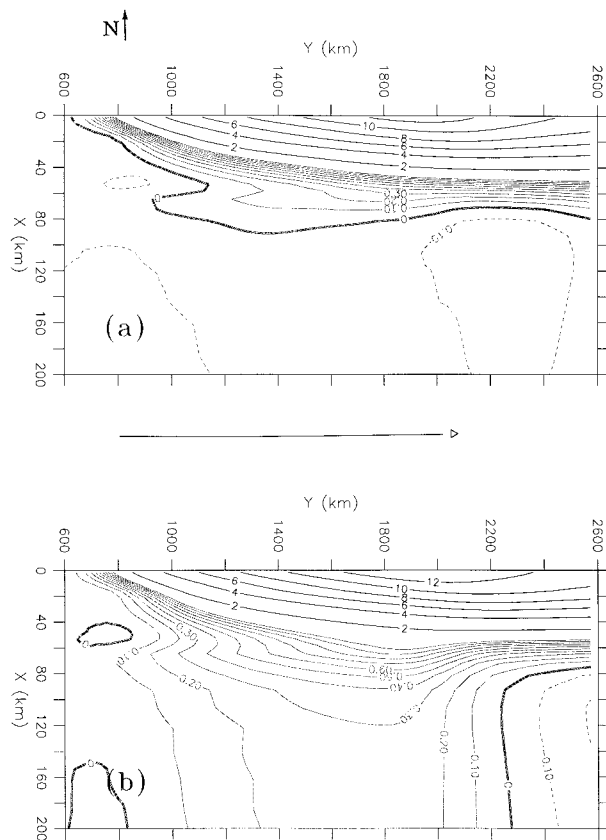
FIG. 3. The sea level field at (a) day 10 and (b) day 30. The contour interval is 2 cm for $\eta \geq 1$ cm and 0.1 cm for $\eta \leq 1$ cm. Dashed contours indicate negative sea level displacement. The direction north (N) is indicated above the panel. The region of wind forcing is indicated below the panel by the arrow and the edge of the shelf is located at $x = 60$ km.

sure gradients and the evolution of the BML. These will be examined in the following section.

To begin, consider the results at day 10 (Fig. 3a), which show that the onshore surface Ekman flux acts to raise sea level by about 12 cm near the coast. By day 30 (Fig. 3b), the sea level pattern within 20 km of the coast has changed little although farther offshore, an alongshore pressure gradient (and cross-shelf flow) has been established, which is shown below to be important to the circulation of the UC.

Below the surface and at section 2, a CC of up to 30 cm s^{-1} is found near the coast that also changes little between days 10 and 30 (Fig. 4). At day 10 a weak UC is found but only at depths greater than 400 m. By day 30, the strength of the UC has increased to about 5 cm s^{-1} (maximum 8 cm s^{-1}), is now found over the shelf slope, and extends to both sections 1 and 3 (Fig. 5). At day 60, the magnitude of the UC doubles to about 10 cm s^{-1} (maximum 15 cm s^{-1}). The continual downwelling also results in an increase in the depth of the BML from about 25 m at day 10, to 50 m at day 30, and 70 m at day 60. Over these times and over the outer

slope, there is a steady increase in the downward tilt of the isopycnals. This tilt, in conjunction with the thermal wind shear within the BML, supports the strengthening of the UC shown in Fig. 4.

Results for the cross-shelf circulation at day 30 are presented in Fig. 6. The results at day 10 are similar. For clarity, the surface mixed layer is excluded from the plot and, as shown, the return flow that is driven by the onshore Ekman flux is downwelling favorable at depths of 150 m or less. Near the shelf and at depths greater than 200 m, the cross-shelf velocities are upwelling favorable. Part of this upwelling is associated with the Ekman transport within the bottom boundary layer and, as shown next, part with the larger scale circulation that is set up by the second mode CTW.

a. A CTW model

A linear, inviscid coastal-trapped wave model for downwelling may be obtained by expanding the pressure field as a sum of orthonormal CTW modes $F_n(x, z)$ such that

$$p = \sum \phi_n(y, t) F_n(x, z), \qquad (1)$$

where $v = (\rho_0 f)^{-1} \partial p / \partial x$, ρ_0 is the average density of the ocean and the ϕ_n satisfy the forced wave equation,

$$\frac{1}{c_n} \partial \phi_n / \partial t + \partial \phi_n / \partial y = b_n \tau^w(y, t) \qquad (2)$$

with c_n the phase speed of the nth mode and $b_n \approx F_n(0, 0) \geq 0$ a coupling coefficient (Clarke 1977). In accordance with the numerical model, we consider a top hat distribution of wind stress

$$\tau^w = \tau_0 \begin{cases} 1, & 0 \leq y^* \leq L_w \\ 0, & \text{otherwise}, \end{cases} \qquad (3)$$

where the transformation $y^* = y - 800$ km shifts the region of wind forcing to lie in the interval $y^* \in [0, L_w]$. The fetch of the wind-forced region is denoted by $L_w = 1200$ km.

Within the wind-forced region, the solution to (2) can be shown to consist of a CTW mode that grows linearly with time and is independent of y^*:

$$\phi_n = c_n t b_n \tau_0, \qquad (4a)$$

until at a time $t = y^*/c_n$, a wave crest arrives from the western end of the forced region. A schematic of the solution is shown in Fig. 7a. After the crest passes, the amplitude is steady and the alongshore pressure gradient that is established, $\partial \phi_n / \partial y^* = b_n \tau_0$, partially balances the force of the wind. At the eastern end of the forcing region the amplitude of each mode is

$$\phi_n(L_w, t) = L_w b_n \tau_0 \qquad (4b)$$

for $c_n t \geq L_w$. Thus, at times before the arrival of the first mode, both η and v are independent of y and grow linearly with time due to the contribution of all modes.
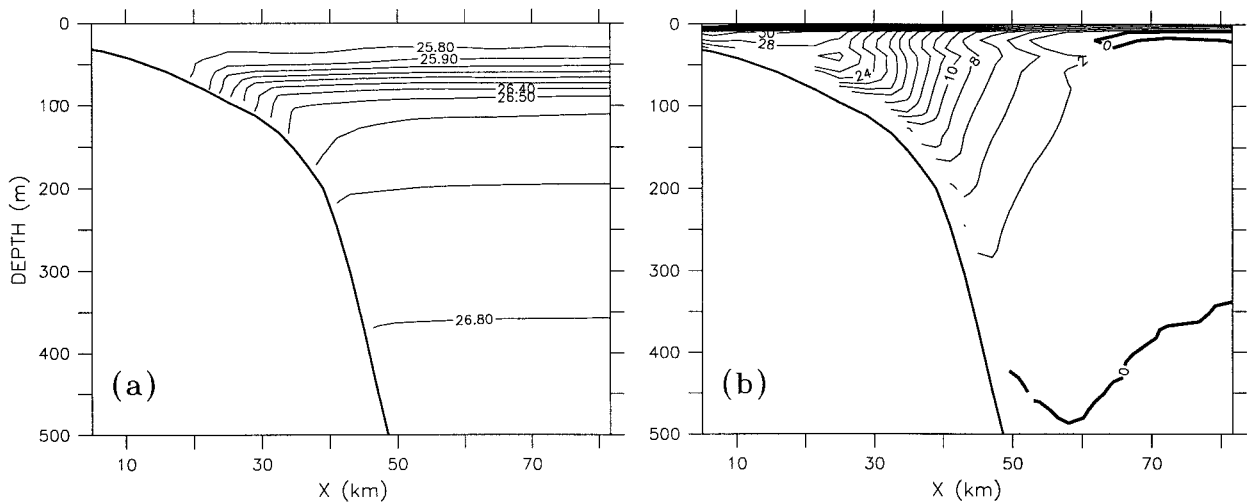
FIG. 4. (a) The density field σ_t at section 2 and at day 10. Units kg m^{-3}, interval 0.1 kg m^{-3}. (b) The alongshore velocity field v at section 2 and day 10. The solid (dashed) contours indicate flow to the east (west). Units cm s^1, interval 2 cm s^{-1}.

Since $u_x + w_z = 0$ at these times, the onshore Ekman flux is largely balanced by a transport away from the coast and the downwelling is two-dimensional in character. After the passage of mode 1, an alongshore gradient v_y is established, but η and v also grow with time because of the higher modes. To the east of the forcing region $\tau^w = 0$, and as shown by the schematic solution (Fig. 7a), the circulation is set up by the arrival of CTWs generated at both the eastern and western ends of the forced region.

To compare these predictions with the numerical results, the first two CTW modal eigenfunctions $F_n(x, z)$ were calculated using the programs of Brink and Chapman (1985). The phase speeds were determined to be $c_1 = 270$ km day^{-1} (3.12 m s^{-1}) and $c_2 = 80$ km day^{-1} (0.93 m s^{-1}) and the coupling coefficients were $b_1 = 0.13m^{-1/2}$ and $b_2 = 0.068m^{-1/2}$.

Now after the passage of the first two modes, coastal sea level at the eastern end of the forced region must satisfy the inequality

$$\eta(0, L_w, t) \geq (L_w \tau_0 / \rho_0 g)[b_1^2 + b_2^2] \qquad (5)$$

since the growing contribution (4a) made by the higher modes is positive. A similar result pertains to the alongshore velocity v and using values calculated for the first two CTW modes, the values of η and v at $(x, y^*) = (0, L_w)$ should exceed 27 and 120 cm s^{-1}, respectively.

The values from the numerical model are much less, with η and v being about 13 cm and 30 cm s^{-1} over days 10–30. The discrepancy here is due partly to bottom drag, which at the coast accounts for about half of the alongshore force needed to balance the wind stress (see Fig. 10a below). Results obtained with bottom drag set to zero show that the alongshore gradient of sea level at the coast increases by a factor of 2, leading to increases in coastal sea level and velocity (see Fig. 11 below). The values obtained, $\eta \approx 20$ cm s^{-1} and $v \approx$

100 cm s^{-1} at $(x, y^*) = (0, L_w)$ and over days 10–30, were again smaller than those predicted by the CTW model.

Despite these discrepancies, the linear CTW model does reproduce some qualitative features of flow evolution. Presented in Fig. 7b is a phase plot of the velocity v obtained near the slope and from the numerical model with bottom drag. Also shown are lines of constant phase for the first two CTW modes. Within the forcing region and at times before the arrival of the first mode, the results are in accord with the CTW result (4a): v increases with time and the alongshore gradients are small. After the passage of the mode 1 wave, an alongshore gradient in v is established in agreement with (4b). The amplitude of the slope velocity v then decreases with time. Part of this decrease may be attributed to the (locally negative) contribution made by the second mode although the arrival of this CTW has little impact on the shelf–slope results for v shown in Fig. 7b. However, an additional feature of the second CTW is that the cross-shelf circulation changes sign near the shelf break and such a result is found both at day 10 and day 30 in the numerical results (Fig. 6).

Beyond day 20 there is no strong evidence of higher mode propagation and, as will be shown, the continued evolution of the UC is due largely to the thermal wind shear that arises from the BML.

b. Net transports

The role of the first mode CTW and evolution of the flow may be further examined by consideration of the net transports through the sections shown in Figs. 1 and 9a. Reference will be made to the schematic of transport and the time line of events shown in Fig. 9b.

Consider first the depth-integrated transport of water hV through section 2 (Fig. 8a). At days 5 and 10, the
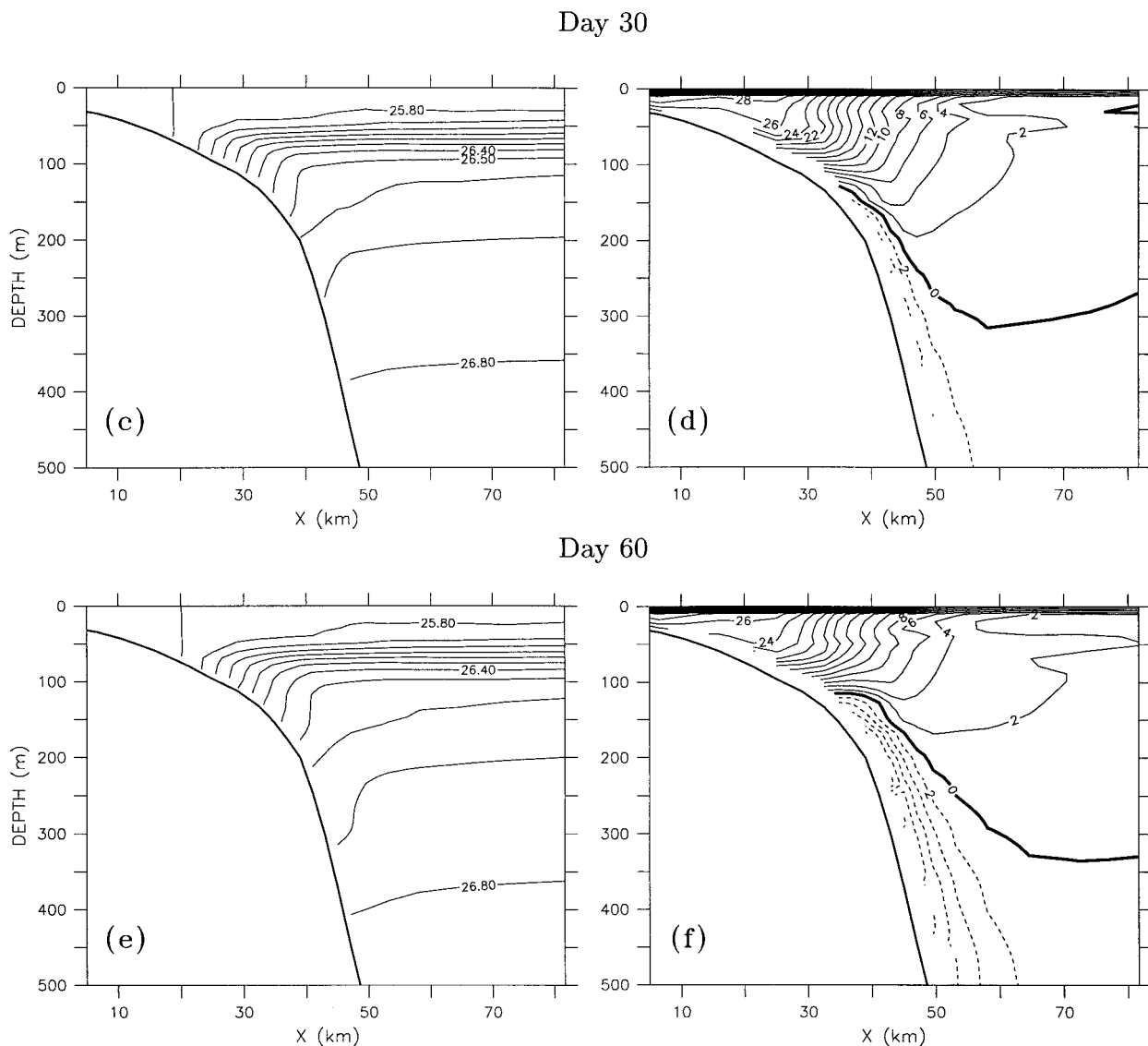
Day 30

Day 60

FIG. 4. (*Continued*) (c) The density field σ_t at section 2 and at day 30: units kg m^{-3}, interval 0.1 kg m^{-3}. (d) The alongshore velocity field v at section 2 and day 30. The solid (dashed) contours indicate flow to the east (west): units cm s^{-1}. (e), (f) As in (c) and (d) but at day 60.

transport is everywhere to the east and changes little with time within 20 km of the coast, indicating that here it is set up largely by the passage of the first CTW mode. Over the slope, however, the growth in the UC leads to a net westward transport by day 30. By day 60, the transport directly associated with the UC is as large as the CC farther inshore.

Now consider results for the net transport $[V] = \int hV \, dx$ (integrated from the coast to $x = 100$ km). Consistent with the model solution shown in Fig. 7a, the arrival of the first mode at section 3 leads to an increase in the transport over the first few days (Fig. 8b). By day 10, the crest generated at the western end of the forcing region has arrived so that $v_y \approx 0$. The growth in the net transport $[V]$ is then substantially reduced, and the

net alongshore transport remains close to 1.2 Sv. In the absence of higher modes, nonlinear and viscous effects, all of the transport supplied by the wind must be carried by the first CTW mode.

Further evidence of the importance of the first mode is given by the transports through sections 1 and 2, which peak at times that correspond to the arrival of the mode 1 crest (day 3 and day 5). At these sections, v_y becomes positive (Fig. 7a), and the net alongshore transports of 0.4 and 0.9 Sv shown in Fig. 8b closely reflect the onshore transport of water that is supplied by the wind (see Fig. 9a).

After day 10, the transport through sections 1 and 2 decreases with time. The decrease here is due to the linear growth of the westward transport associated with
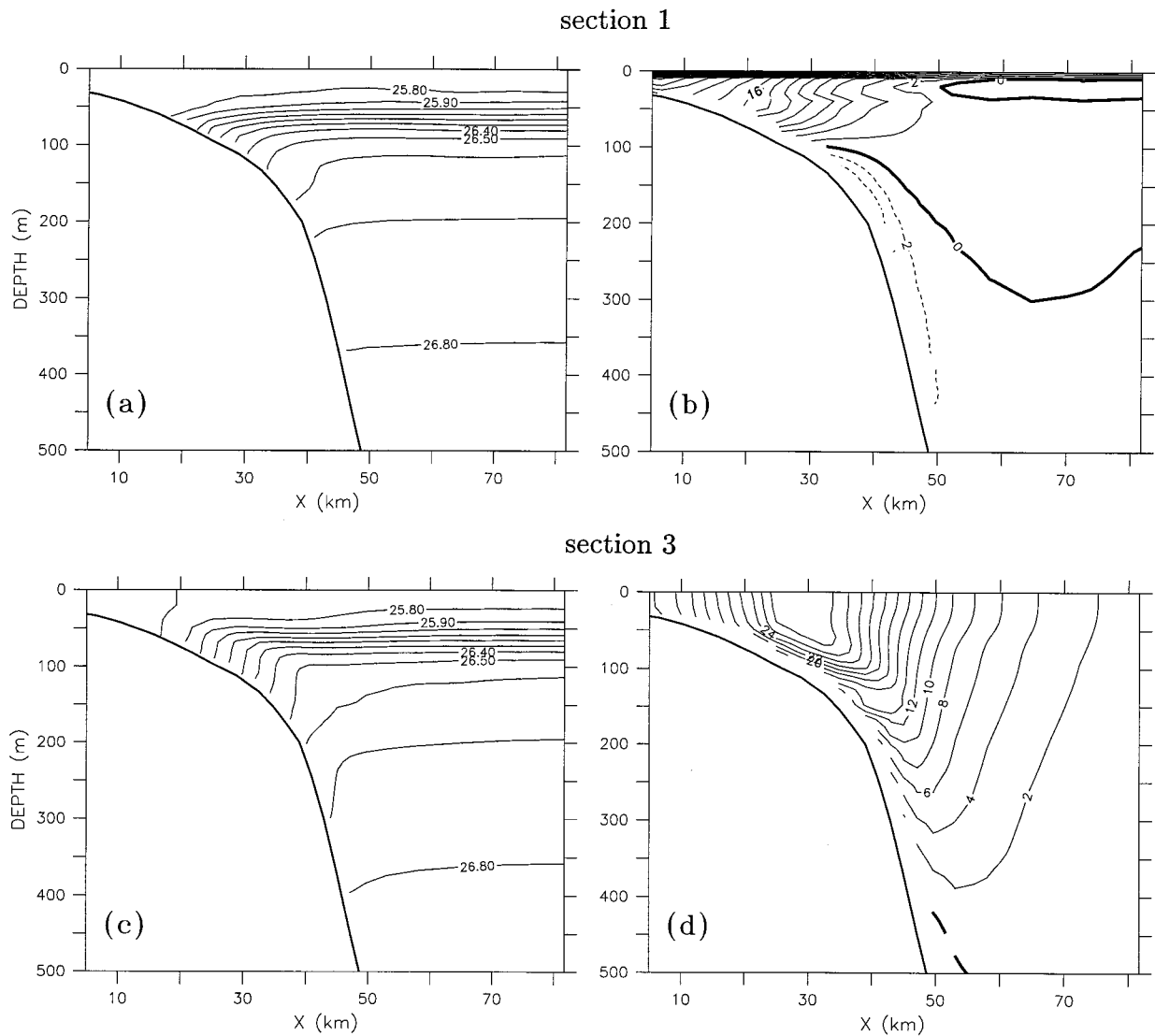
section 1

section 3

FIG. 5. (a) The density field σ_t at section 1 and at day 30; units kg m^{-3}, interval 0.1 kg m^{-3}. (b) The alongshore velocity field v at section 1 and day 30. The solid (dashed) contours indicate flow to the east (west): units cm s^{-1}, interval 2 cm s^{-1}. (c), (d) As in (a) and (b) but at section 3.

the UC (Fig. 8b), which by day 60 amounts to about 0.5 and 0.7 Sv at sections 1 and 2. The corresponding transports of the CC are therefore 0.4 and 0.9 Sv, respectively, and essentially unchanged from the values at around day 10. That is, the alongshore divergence of the CC accounts for nearly all of the mass flux that is driven onshore by the wind. These estimates are presented in the schematic shown in Fig. 9a.

Next consider cross-shelf transports through sections 4, 5, and 6. To facilitate the analysis, we define a cross-shelf residual transport hU_r to be the total transport, less the onshore surface Ekman transport (hU_E). Results for the *net* transport $\langle U_r \rangle = \int hU_r \, dy$ through sections 4, 5, and 6, are presented in Fig. 8c. At section 4, the residual cross-shelf transport is near zero over the first 10 days

since the early passage of the first CTW crest sets up a divergence, $v_y \geq 0$, which absorbs the onshore surface Ekman transport.

At section 5, the CTW arrives later so that from the model solution (4a), initially $v_y \approx 0$, and the offshore residual transport of about 0.4 Sv simply reflects the 0.5 Sv that is supplied by the wind. With $hU_r \approx -hU_E$ and $v_y \approx 0$, the downwelling over this initial period is two-dimensional in nature as indicated by the time line (Fig. 9b). By day 10 and following the arrival of the first CTW, the surface Ekman transport is again absorbed by the alongshore CC and the residual offshore transport drops to near zero.

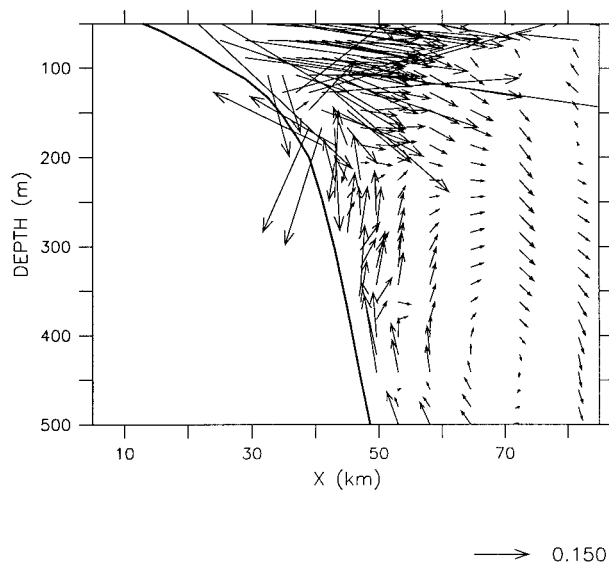Section 6 encompasses part of the region of wind forcing so that the offshore transport is driven by the

FIG. 6. The $(u, 100w)$ vector field at section 2 and day 30. A vector of length 0.15 cm s^1 vector is indicated.
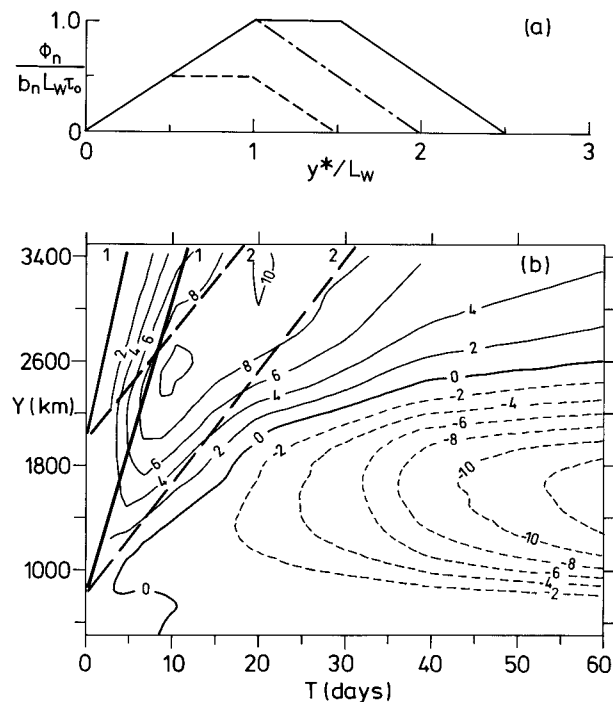

FIG. 7. (a) The CTW model solutions (4) for ϕ_n as a function of the alongshore distance y^* from the western end of the forcing region, and at times given by $c_n t = L_w/2$ (short dashed), $c_n t = L_w$ (long-short dashed), and $c_n t = 3L_w/2$ (solid). (b) A phase plot of the alongshore velocity obtained from the numerical model and over the slope at $(x, z) = (44$ km, 245 m). The solid (dashed) contours indicate flow to the east (west): units cm s^{-1}, interval 2 cm s^{-1}. The straight lines labelled 1 (solid) and 2 (dashed) denote the lines of constant phase for the mode 1 and 2 CTWs that emanate from the western and eastern ends of the forcing region.

surface flux and by the alongshore divergence of the CC in the unforced region. Again, the transport falls to near zero upon arrival of the first mode CTW that is generated at the western end of the forcing region.

While the initial transports are consistent with first mode dynamics, at later times they are dominated by the linear growth of the UC. By day 60 for example, the transports through sections 4 and 5 and through section 6 are respectively directed away and toward the shelf (Fig. 9a) and the values are consistent with the alongshore divergence of the UC. The onshore transport of 0.8 Sv through section 6 is largely redirected into the westward UC and, in turn, is drained offshore through sections 4 and 5. These cross-shelf transports are geostrophically supported by the alongshore gradients of sea level illustrated in Fig. 3b.

These results suggest little exchange between the CC and UC, and estimates of upwelling based on the vertical velocity (300-m depth) indicate transports of only 0.03 and 0.06 Sv through the horizontal sections $(x, y) \in$ ([0, 100], [600, 1200]) and $(x, y) \in$ ([0, 100], [1200, 1700]). Thus at zeroth order, the alongshore divergence of the CC can be accounted for by the supply of water from the surface Ekman flux, while within the forced region, the alongshore divergence of the UC leads to a cross-shelf circulation.

Finally, we return to the results for the cross-shelf velocity (Fig. 6), which over the shelf slope and within the BML, are notably chaotic in appearance. Results (not presented) show that the fluid is rising and falling along isopycnal surfaces within the BML and the circulation here has the characteristics of a slantwise convective instability (Emanuel 1994). Such an instability was found by Allen and Newberger (1996) in a simulation of two-dimensional downwelling. Here the con-

ditions for the instability are met including a change in the sign of the potential vorticity. The cross-shelf scale of the instability is of order v/f (Emanuel 1994), or 1 km assuming $v = 10$ cm s^{-1} for the shelf break region. The instabilities are not well resolved since the model grid size $\Delta x \approx 2$ km is larger than the scale of the instability. In light of this, and the fact that the instabilites do not seem to have any impact on the larger scale circulation, no further discussion is made.

4. Dynamics: The role of the bottom mixed layer

Here the role of the BML and bottom friction in determining the circulation is examined. In particular, it is shown that the thermal wind shear associated with the BML is important to the UC, while variations in the rapidity of shutdown of bottom stress and arrest of BML transport can lead to the detachment of flow into the interior and a further downwelling of isotherms. While bottom friction does become small over the slope, it is nonetheless shown to be important nearer the coast in determining the overall cross-shelf transport, degree of downwelling, thermal wind shear, and magnitude of the UC. An explanation for the cause of the UC is given
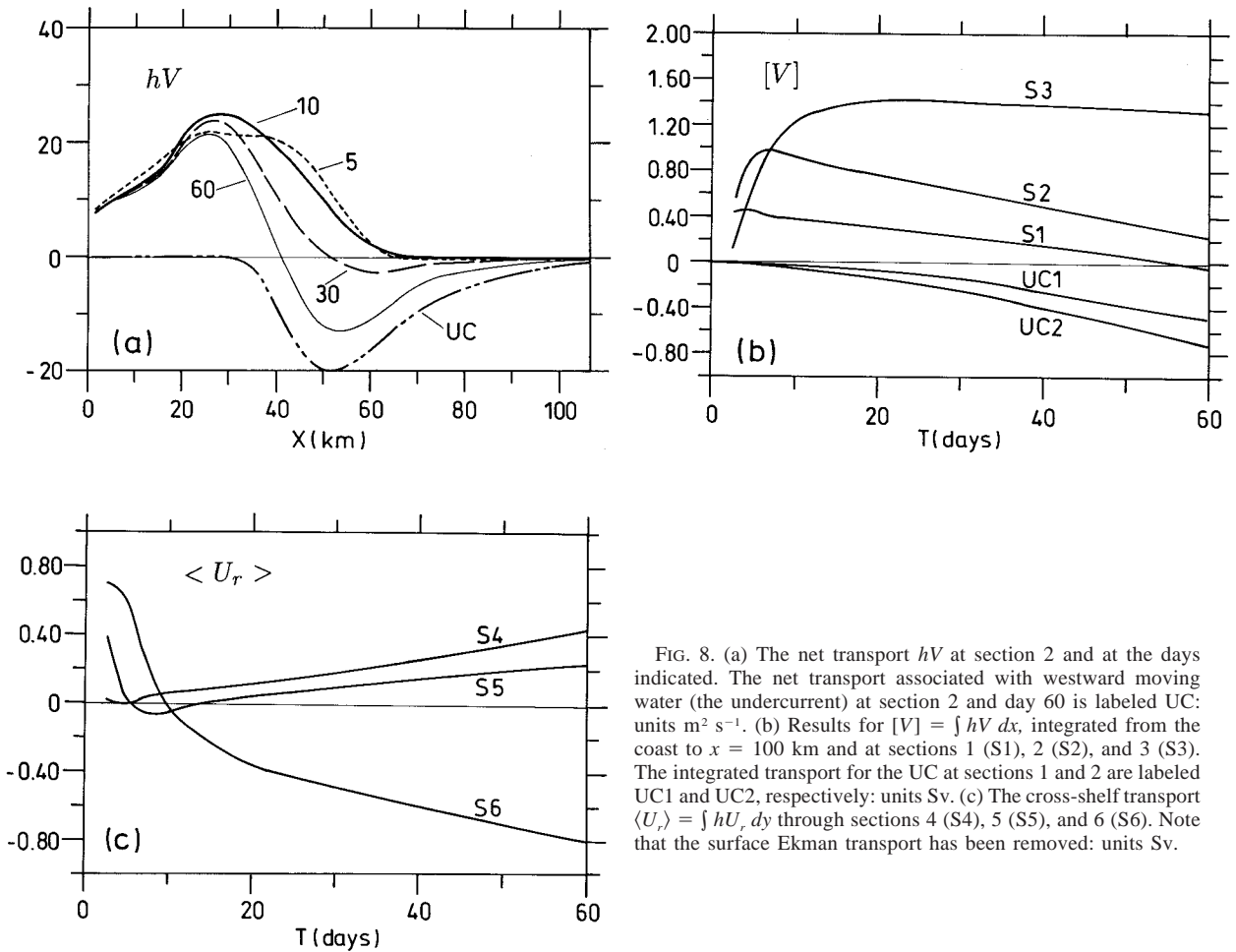
FIG. 8. (a) The net transport hV at section 2 and at the days indicated. The net transport associated with westward moving water (the undercurrent) at section 2 and day 60 is labeled UC: units m^2 s^{-1}. (b) Results for $[V] = \int hV \, dx$, integrated from the coast to $x = 100$ km and at sections 1 (S1), 2 (S2), and 3 (S3). The integrated transport for the UC at sections 1 and 2 are labeled UC1 and UC2, respectively: units Sv. (c) The cross-shelf transport $\langle U_r \rangle = \int hU_r \, dy$ through sections 4 (S4), 5 (S5), and 6 (S6). Note that the surface Ekman transport has been removed: units Sv.

and the evolution of the flow far from the forcing region examined.

To facilitate the analysis, terms in the depth-integrated momentum equations will be presented for section 2 and at day 30. In particular with g the acceleration due to gravity, and the pressure due to density (σ) denoted by

$$p' = g \int_z^0 \sigma \, dz, \qquad (6)$$

the depth-integrated momentum equations may be approximated by

$$\rho_0 h \partial U / \partial t = \rho_0 f h V - \rho_0 g h \eta_x - h P_x \qquad (7a)$$
$$\text{CFX} \qquad \text{SGX} \qquad \text{DGX}$$

and

$$\rho_0 h \partial V / \partial t = -\rho_0 f h U_r - \rho_0 g h \eta_y - h P_y - \tau^b, \qquad (7b)$$
$$\text{CFY} \qquad \text{SLY} \qquad \text{DGY} \quad \text{BSY}$$

where the depth-average of (u, v) and (p'_x, p'_y) are denoted by (U, V) and (P_x, P_y). The (negligible) bottom

friction term in (7a) has been deleted, but retained in (7b). Nonlinear and horizontal diffusion terms are neglected. The sum of the right-side terms, while generally small, is presented below. In (7b), the alongshore wind stress τ^w has been subtracted from the Coriolis term and results for the (residual) Coriolis force, CFY = $-\rho_0 f h U_r$ are presented.

The labels used for each term in the plots are indicated above and with a change of sign, the forces SGX = $-\rho_0 g h \eta_x$ and DGX = $-h P_x$, are also measures of the gradients of sea level and density. In the following, the sign change is taken to be understood when both these and the alongshelf forces SGY and DGY are referred to as gradients.

Now consider the nearshore region, $x \lesssim 20$ km, where the water is well mixed (Fig. 4). From Fig. 10b, CFX + SGX ≈ 0 so that the cross-shelf balance is strongly barotropic and geostrophic:

$$fV = g \eta_x, \qquad (8a)$$

while the results in Fig. 10a show that CFY + SGY + BSY ≈ 0 and the alongshore wind stress is approxi-

mately balanced by the retarding forces that arise from friction and the gradient of sea level,

$$\rho_0 f h U \approx 0 \approx -\rho_0 h g \eta_y + \tau^w - \tau^b. \quad (8b)$$

a. The role of the bottom mixed layer

Over the shelf slope ($x \gtrsim 40$ km), downwelling leads to cross-shelf density gradients (DGX) that are of similar magnitude to the large opposing sea level gradients (SGX) and an UC is present. The maximum in the depth-integrated density gradient (DGX) occurs at ($x \approx 48$ km) while the maximum of the *depth average* (not shown) occurs farther inshore at ($x \approx 36$ km) and near the top of the UC. The density gradients here arise from the downwelled isopycnals within the BML and the inviscid interior. The contribution made by the shear within the BML to the depth-integrated density gradient is large and can be estimated from

$$\text{DGX}_B = -\frac{g h_B^2}{2} \partial \sigma_t / \partial x \quad (9)$$

if $\partial \sigma_t / \partial x$ is constant over the BML, height h_B. For section 2 and at $x = 36$ km, the numerical results show that $\partial \sigma_t / \partial x$ is about 3.5×10^{-5} kg m^{-4}, while the results in Fig. 4d indicate the BML height to be about 70 m. The gradient DGX_B is then about -0.9 Pa or 75% of the total -1.2 Pa shown in Fig. 10.

Farther offshore, the density gradient is larger due to the increased tilt of isopycnals over the slope and spreading of isopycnals near the shelf break (Fig. 4). The spreading results from the convergence and detachment of the cross-isobath flow near the shelf break (Fig. 6) and is similar in appearance to that found by Gawarkiewicz and Chapman (1991). They considered the evolution of a vertically uniform inflow along a linearly stratified shelf and found the bottom Ekman transport over the shelf to be blocked at the shelf break and redirected into the interior. In their case, the blocking occurs because the bottom Ekman transport over the steep slope is effectively arrested due to thermal wind shutdown within the BML. In terms of scales for shutdown, the Burger number S and effective stratification are larger over the steeper slope so that the timescale for shutdown $T_S = (S + 1)/(C_D N S^{3/2})$ is smaller (Garrett et al 1993; Middleton and Ramsden 1996). The arrest of the Ekman transport over the steep slope occurs well before the arrest over the inner shelf and the flow within the BML is driven into the interior.

Here, the detachment of the cross-isobath flow near the shelf break arises from the convergence of the offshore and upwelled circulation shown in Fig. 6 and from the near arrest of the Ekman transport over the slope. The latter is illustrated in Fig. 11 by the results for $h U_b = -\tau^b/\rho_0 f$, the offshore transport within the BML. Note that at day 30, the surface and bottom boundary layers merge within 25 km of the coast so that $h U_b$ is only a useful measure of transport farther offshore. Over these distances the transport does change sign indicating a convergence and detachment of flow near the shelf break.

The results in Fig. 11 also show that the bottom transport and stress are more rapidly shutdown over the slope ($x \gtrsim 30$ km) where the Burger number becomes large (Fig. 2). The shutdown of bottom stress by the BML is also enhanced by the thermal wind shear of the overlying isopycnals as shown by the calculation based on (9) above. About 25% of the integrated thermal wind shear at $x = 36$ km was found to arise from the tilt of isopycnals above the BML.

Models for the downwelled BML have been developed assuming a constant slope, stratification, and interior alongslope current. For example, Garrett et al. (1993) have shown that over several shutdown scales T_S, the BML height should grow toward a value of $h_D = v_i/N S^{1/2}$, where v_i is the alongslope velocity above the boundary layer. Such models are only of qualitative use in describing the BML here since the slope, stratification, and alongshore current are not uniform and the latter evolve with time. For example, the $26.4 \sigma_t$ curve shown in Fig. 4e is advected and downwelled by 10 km and 70 m from the initial state.

Nonetheless, let us estimate these BML scales for the $26.4 \sigma_t$ isopycnal, which lies initially at a depth of 80 m and intercepts the shelf at $x = 20$ km. Using the values of $S = 0.2$ and $N = 0.01$ at this point, we obtain $T_S \approx 6$ days and $h_D \approx 38$ m. A value of $v_i = 17$ cm s^{-1} is taken from the numerical results at section 2. The shutdown scale is perhaps consistent with the reduction in bottom stress shown in Fig. 11, although the predicted height is about half the 70 m found from the numerical model. These predictions can be improved if estimates of the stratification within the BML at day 30 are used. Assuming the scaling $\sigma_x = \sigma_z h_x$ and the value for σ_x noted above for the BML at $x = 36$ km, we obtain values of $N = 0.006$, $S = 0.34$, $T_S \approx 5$ days, and $h_D \approx 50$ m. The choice of stratification and slope is somewhat arbitrary.

The events above are summarized in the time line (Fig. 9b). Over the first 10 days, the dynamics is dominated by a CTW phase and a quasi-steady circulation is set up near the coast. The shutdown of bottom stress begins soon after day 5 and is complete by day 30, leading to the detachment of BML water into the interior and spreading of isopycnals. Indeed, after day 10, the slope dynamics is characterized by a BML phase: the thermal wind shear and UC over the slope increase linearly with time due to the growth of the BML and, to a lesser extent, due to the increasing tilt of isopycnals in the interior.

To further examine the role of the bottom friction and the BML, results were obtained with the bottom drag coefficient C_D set to zero (Fig. 12). In this case, the downwelling over the slope and magnitude of the UC are much weaker than where the BML was present (Fig. 4c), while near the coast, the CC and cross-shelf gradient
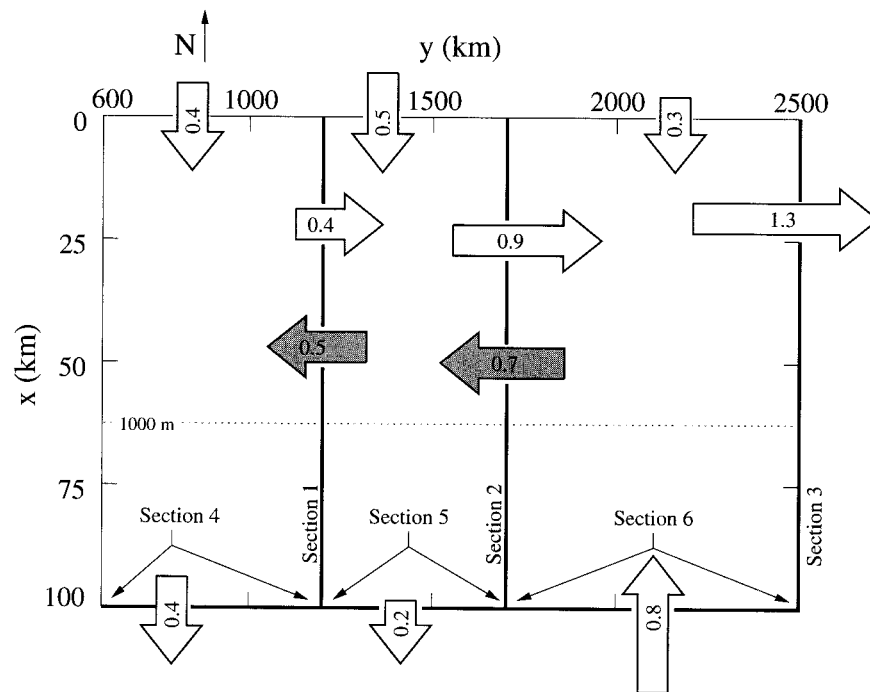
FIG. 9. (a) A schematic of the net transports (units Sv) through sections 1 to 6 at day 60. The direction north (N) is indicated above the panel. The eastward and westward directed arrows indicate the transport associated with the coastal current and undercurrent (shaded). The offshore transports are indicated at the bottom of the panel. The transports indicated at the coast (top of the panel) correspond to the return flow driven by the wind-forced Ekman transport. The vertical transport to the west of section 2 and at a depth of 300 m is estimated to be about 0.1 Sv.

of sea level are much larger. The explanation for these results may be gleaned from the momentum balances shown in Figs. 10 and 12. In the absence of bottom drag, the current v accelerates so as to balance wind stress. This leads to a larger alongshore velocity and divergence v_y, which is fed primarily by water supplied by the offshore transport hU_r. The reduction in the transport across the shelf is illustrated in Fig. 12c where at $x = 25$ km, $\rho_0 fhU_r = CFY$ is about half that obtained where friction is present (Fig. 10a).

Downwelling over the shelf is thus larger in the case where bottom drag is *nonzero,* and leads to a density gradient over the slope that is 2–3 times larger than that obtained with zero bottom drag. The sea level gradient is also 2–3 times larger when bottom drag is present since more of the CC lies over the slope. Through geostrophy, the larger cross-shelf gradients of sea level and density support a larger UC.

b. The cause of the undercurrent

The presence of an UC in the results above may be contrasted with the two-dimensional circulation obtained when alongshore variations are precluded. The results of Mellor (1986) and Allen and Newberger (1996) show that under these conditions, a UC does not develop for downwelling (or upwelling) favorable flows and v is everywhere in the direction of the wind. The reason given here is that, since $v_y = 0$, the onshore surface Ekman transport leads to an offshore transport everywhere within the interior. The alongshore momentum equation reduces to $d[v + fX]/dt = 0$ in the inviscid interior and, since the fluid parcel displacements X are positive, $-v/f$ and v must be positive and the latter in the direction of the wind. (Recall that f is negative.) Moreover, since v is positive and nearly geostrophic, the pressure gradient due to sea level must be greater than that due to density:

$$-\rho_0 g\eta_x \geq p'_x. \quad (10)$$

In the fully three dimensional results above, alongshore gradients exist so that the constraint (10) is relaxed, the pressure gradient due to density can exceed that due to sea level, and a UC can exist. Thus, a necessary condition for a UC is that the wind act over a finite or semi-infinite fetch so that alongshore pressure gradients can exist.

The pressure gradient necessary to drive the UC can be gleaned from the alongshore momentum terms presented in Figs. 10c and 10d. At day 10 and at a depth of 50 m, the Coriolis force $(-fu)$ due to the downwelling exceeds that due to sea level $(-g\eta_y)$, and thus acts to
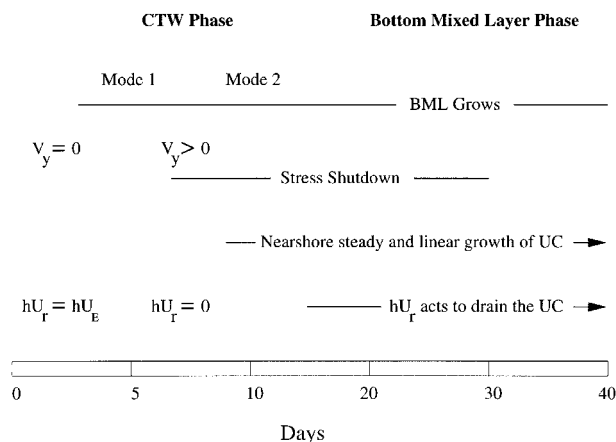
FIG. 9. (*Continued*) (b) A time line illustrating the events in the circulation at section 2. (The timescale is not linear.) Before the arrival of the first CTW at day 5, the downwelling is essentially two dimensional and the onshore Ekman transport hU_E is mostly directed offshore into hU_r. After day 5, hU_E is redirected into the now divergent alongshore coastal current. The nearshore zone becomes quasi-steady upon arrival of the second mode CTW at around day 10. This mode also sets up a weak UC, which then grows due to the increasing thermal wind shear associated with the BML and interior isopycanal tilt. The alongshore divergence of the UC drives an offshore transport hU_r through section 5 and onshore transport through section 6.

accelerate the CC (Fig. 10c). The alongshore pressure gradient due to density is negligible at this depth. After day 10, the downwelling and acceleration become smaller and as noted above, the CC becomes quasi steady.

Now consider the results in Fig. 10d obtained at a depth of 150 m. Results are presented for day 30 since at this time the alongshore gradient due to density is significant and bottom stress and frictional effects are negligible. As shown, the alongshore gradient of sea level over the slope, $x \in (35, 50)$ km, is larger than the sum of the Coriolis force ($-fu$) and density gradient ($-p'_y/\rho_0$) since the downwelling and u diminish with depth. The alongshore gradient of sea level thus drives the UC, although through geostrophy, the magnitude is also determined by the degree of thermal wind shear. Indeed, without thermal wind shear, no UC could arise and the momentum balance would be just that given by (8): the alongshore current would be everywhere in the direction of the wind, while the alongshore gradient in sea level would be balanced by frictional stresses.

c. The far field

The behavior of the velocity field far from the forcing region is also of interest. Results at $y = 3000$ km (not presented) show the solutions for both σ_t and v to be very similar to those for section 3 although friction does act to spread the maximum in the alongshore velocity a little more across the shelf. The amplitudes of the alongshore pressure gradients, bottom friction, and

cross-shelf transport (CFY $= \rho_0 fhU_r$) are similar and small at these sections being within 0.2 Pa or ¼ of that found within the forcing region.

Similar results were reported by Chapman and Lentz (1997), who found that an initially narrow along-isobath current will spread across the shelf due to transport within the bottom boundary layer. As this layer grows in height, the associated thermal wind shear reduces bottom stress and cross-shelf Ekman transport until an equilibrium state is reached where bottom stress is completely shutdown and the boundary layer transport is arrested. For the results here, the shutdown of bottom stress and cross-shelf transport is not complete, although the conclusion is the same. A quasi-equilibrium state results in which the effects of bottom friction are small and the alongshore current can flow unimpeded over many hundreds of kilometers.

While these comments relate to the circulation outside of the forcing region, a striking feature of the solutions is that the details of the density field within the BML at section 3 (Fig. 5c) are almost identical to those at section 2 (Fig. 4c). Section 2 lies 800 km to the east of section 3 and 300 km inside of the forcing region. The alongshore velocity field at the two sections is quite different, so the sea level fields must also be different.

The explanation for the similarity of the density field may involve the downwelling and mixing that should result from the adjustment of any along-isobath variations in density. For example, suppose that within the wind-forced region, the isopycnals are downwelled to form a BML and are in geostrophic balance with an along-isobath current. Assume also that the isopycnals are flat to the east of the forced region. Now in the absence of an opposing sea level gradient, the relatively dense fluid in the east will accelerate toward the BML, be deflected into deeper water by the Coriolis force and then mix vertically until the along-isobath density gradient is eliminated. The downwelling then ceases and, once the water is mixed, it does not restratify immediately. Rather, it remains locked in a state of thermal wind balance even if the overlying alongshore current changes in time (Middleton and Ramsden 1996). Through this process, the BML will tend to replicate itself along the shelf and in the direction of CTW propagation. Note that this adjustment process cannot occur to the west of the forced region since dense water would be deflected into shallower and not deeper water.

The adjustment of alongshore variations in sea level will also give rise to a cross-isobath velocity, although unlike density, there is no process of advection and mixing to eliminate the along-isobath gradient. Rather, such an along-isobath gradient can be maintained through a geostrophic balance with the Coriolis force associated with the cross-isobath velocity.

5. The effect of varying parameters

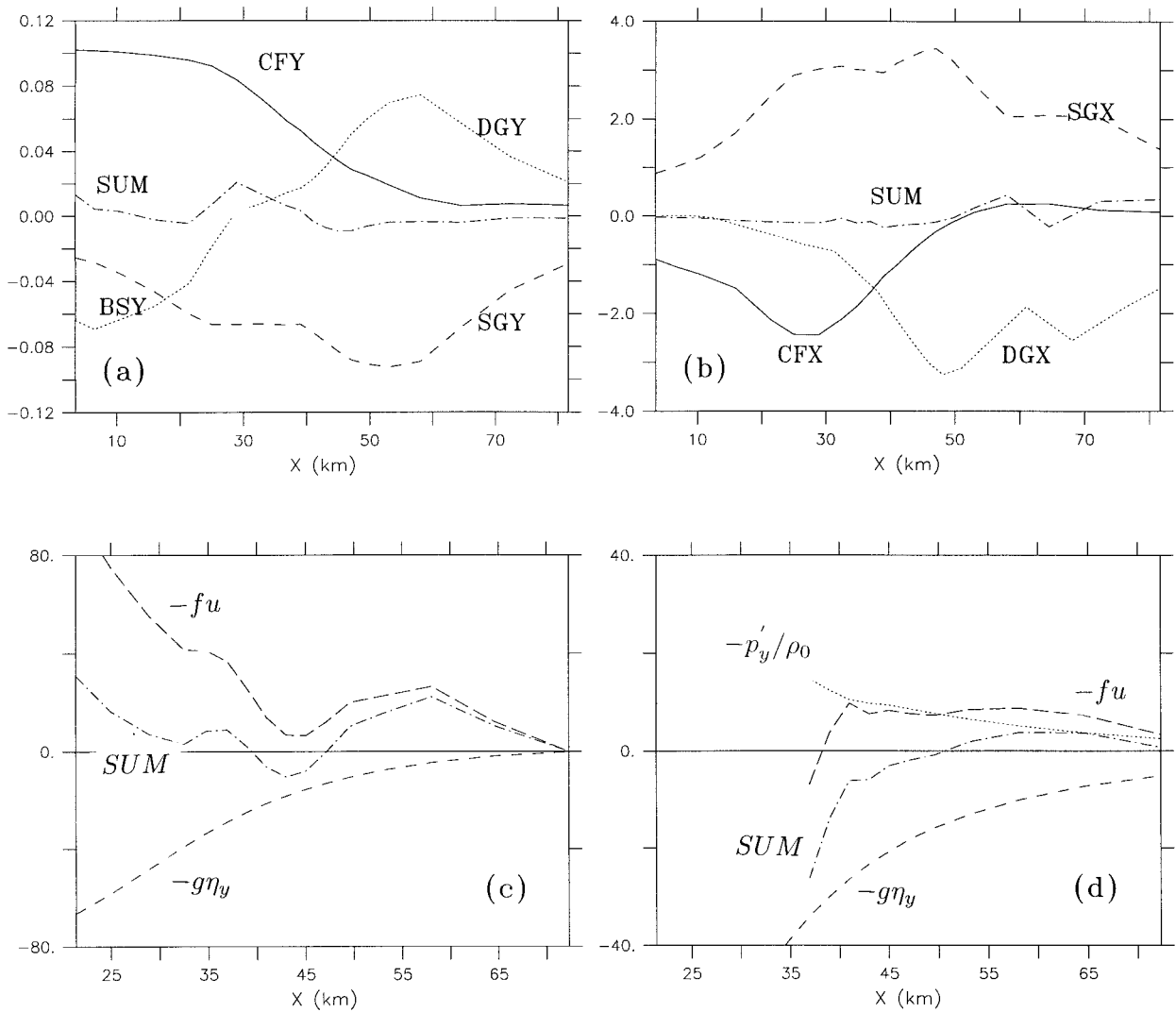Here we consider the effects of spatial variations in the Coriolis parameter and wind stress and the sensi-

FIG. 10. (a) Results for the integrated alongshore momentum equation at day 30 and for section 2 (units, Pa). Indicated are the Coriolis force (CFY) associated with the residual cross-shelf transport U_r, the force (SGY) due to the alongshelf gradient of sea level, the force (DGY) due to the alongshore density gradient, the alongshore bottom stress (BSY), and the sum (SUM). Note that DGY is near zero for $x \leq 30$ km while BSY is near zero for $x \geq 30$ km. (b) Results for the integrated cross-shelf momentum equation at day 30 and for section 2 (units, Pa). Indicated are the Coriolis force (CFX), the force (SGX) due to the cross-shelf gradient of sea level, the force (DGX) due to the cross-shelf density gradient, and the sum (SUM). (c) Day 10 results for the alongshore momentum terms $-fu$, $-g\eta_y$, and their sum at a depth of 50 m and for $y = 1500$ km, (units, $10^{-8} \times$ m s^{-2}). (d) Day 30 results for the alongshore momentum terms $-fu$, $-g\eta_y$, $-p'_y/\rho_0$ and their sum at a depth of 150 m and for $y = 1500$ km (units $10^{-8} \times$ m s^{-2}).

tivity of results to the stratification and bathymetry. Our first goal is to examine the dynamical consequences of such variations relative to the basic downwelling case above and the upwelling results of Suginohara and Kitamura (1984). We also wish to examine these effects in the context of the wind-forced shelf circulation of the Great Australian Bight. However, since the stratification, bathymetry, and wind stress vary considerably within the bight, our aim here is to ascertain the qualitative nature of these effects rather than to provide an exact diagnosis of the shelf circulation.

a. Positive wind stress curl

Alongshore winds within the bight (and in many other regions) increase in strength with distance from the coast. To investigate the effects of a positive wind stress curl, we follow McCreary and Chao (1985) and let the stress distribution shown in Fig. 1 increase linearly with distance from the coast:

$$\tau^w = \tau_0 \begin{cases} 0.5[1 + x/L_s], & 0 \leq x \leq L_s \\ 1.0, & x > L_s, \end{cases} \quad (11)$$
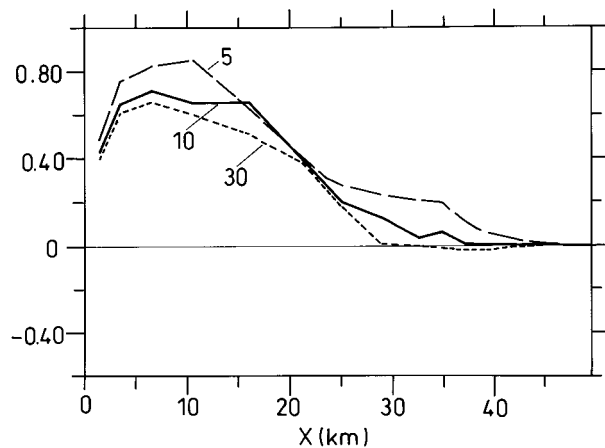
FIG. 11. The offshore transport $hU_b = -\tau^b/(\rho_0 f)$ as indicated by the alongshore bottom stress τ^b at section 2 and at the days indicated: units $m^2 s^{-1}$.

where $\tau_0 = 0.1$ Pa and $L_s = 60$ km denotes the width of the shelf. The stress distribution will lead to a 50% reduction in the nearshore surface Ekman transport and the numerical results (not presented) show a 30% reduction in coastal sea level relative to the basic curl-free case (Fig. 3). The amplitude of the nearshore CC is also reduced by a similar amount (Fig. 13b) and the net reduction in the offshore transport below the surface mixed layer leads to a reduction in the downwelling of isopycnals (Fig. 13a).

The reduction in downwelling is offset by the Ekman pumping associated with the curl of the wind stress. Over the shelf slope ($x \geq 40$ km), the pumping acts to tilt the isopycnals down and raise sea level, and the cross-shelf gradients of sea level and density are much larger than those found in the curl-free case (Fig. 10b). Through geostrophy, these larger gradients support an intensification and spreading of the CC near the surface (Fig. 12b) and a UC that is similar to that found in the curl-free case (Fig. 4d).

By day 60, the CC and UC are similar to that shown in Fig. 4f, but spread farther across the shelf since the Ekman pumping leads to a general tilt in both sea level and isopycnals. In the curl-free case the UC is narrower since the thermal wind shear near the shelf is larger due to the thicker BML and spreading of isopycnals.

b. Wintertime stratification

As noted in the introduction, a feature of the wintertime stratification within the bight is the presence of relatively light water over much of the shelf, while farther offshore a surface mixed layer 100 m deep results from mixing and cooling. Possibly, the results obtained using using the summertime stratification may be more indicative of the wind-forced currents during winter. In any case, it is worth determining the sensitivity of the results to the density field and solutions were obtained

using a wintertime stratification (Levitus and Boyer 1994; Levitus et al. 1994) and for the South Australian region (Fig. 14a).

With no other changes to the basic case, the results at day 30 show that the presence of the deep surface mixed layer leads to a reduction in downwelling and in the magnitude of the UC. The latter is reduced to speeds of 1 cm s^{-1} and is only found at depths of more than 400 m. The near elimination of the UC results from the absence of the summertime thermocline and associated thermal wind shear within and above the BML. From Fig. 14d, the cross-shelf density gradient DGX is about -0.2 Pa at $x = 36$ km and much smaller than the summertime value of -1.2 Pa (Fig. 10b).

The results in Fig. 14 also show that the CC and gradients of sea level and density are generally smaller than found in the original summertime case. The simplest explanation for the weaker CC is that in the absence of the summertime thermocline, shutdown over the shelf is precluded and more energy is dissipated by the increased bottom drag. In the basic summertime case, thermal wind shear led to a bottom stress BSY that was zero at $x = 30$ km. Here, the stress at $x = 30$ km is nonzero and leads to a decrease in the alongshore gradient of sea level since both must approximately balance the Coriolis force CFY. The reduction in the alongshore gradient of sea level in turn leads to a reduction in the cross-shelf gradient SGX and velocity v.

c. Bathymetry

Within the bight, the width of the shelf can vary from 40 km to more than 200 km. To illustrate the effect of a wider shelf, an extra 25 km of linearly sloping shelf was added to that above and between the depths of 50 and 100 m. Using the summertime stratification, the results obtained (Fig. 15) show that the nearshore velocity v is similar to that found in the original case. Farther offshore, the circulation is generally weaker and near the shelf break ($x \approx 65$ km), the near surface CC and gradient SGX are about 7 cm s^{-1} and 1.4 Pa or 40% smaller than found in the original case. The UC is also reduced in magnitude.

The explanation for these results involves the wider shelf, which effects the circulation in two ways: First, vertical mixing within 40 km of the coast eliminates thermal wind shear and leads to an increase in drag over more of the shelf (Fig. 15c). The circulation is weakened. Second, since the (divergent) alongshore transport of the CC is spread over a shelf of greater width, the associated sea level gradient SGX and cross-shelf transport near the shelf break are reduced. For example, the results for CFY in Fig. 15 ($x = 65$ km) indicate a 30% reduction in hU_r relative to that shown in Fig. 10 ($x = 40$ km). Downwelling and the cross-shelf density gradient are reduced by a similar amount, but a UC results that is similar to that found in the basic case since the
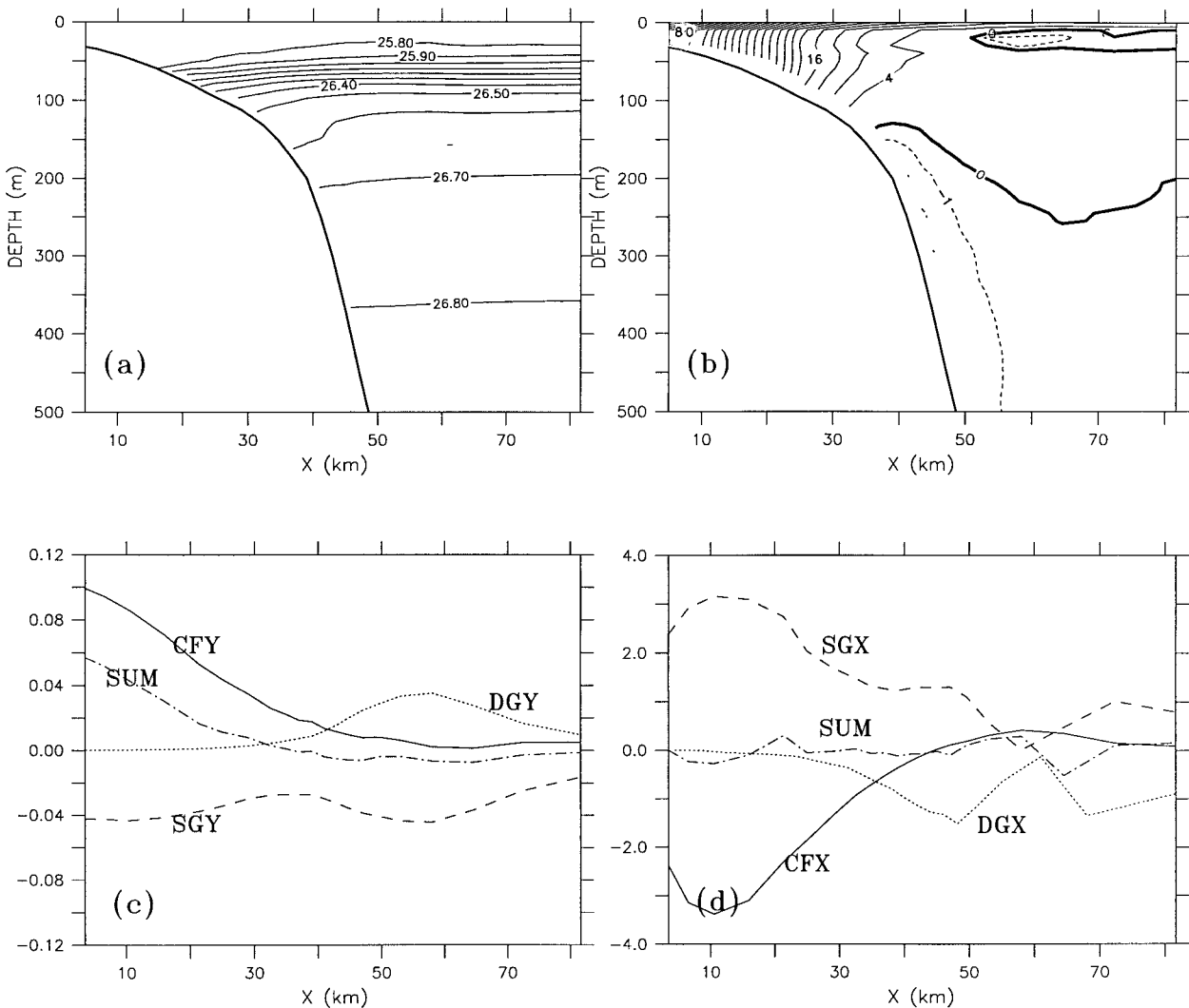
FIG. 12. Results obtained at day 30 and for section 2 but with bottom drag set to zero. (a) The density field σ_t at section 2 and at day 30: units kg m^{-3}, interval 0.1 kg m^{-3}. (b) The alongshore velocity field v at section 2 and day 30. The solid (dashed) contours indicate flow to the east (west). Units cm s^{-1}. Note that the contour interval is 4 cm s^{-1} (1 cm s^{-1}) for flow to the east (west). (c), (d) Results for the alongshelf and cross-shelf integrated momentum equations at section 2. The labels are described in Fig. 10 and in the text.

opposing contribution made by the sea level gradient SGX is also reduced.

These results may be extrapolated to a very wide shelf such as that found in the central region of the bight. For such a shelf, the cross-shelf transport that is driven by the wind may be spent over the shelf in supplying water to the divergent CC. Near the shelf break the offshore transport may be near zero and a wind-forced UC may not exist.

d. The beta effect

While the bight is predominantly zonal, the shelf veers some 900 km to the south at the eastern end so that Rossby wave dispersion of energy may be significant. In an upwelling study, Suginohara and Kitamura (1984) found that such dispersion led to a strengthening of the UC. They chose a β plane centered on the Coriolis parameter $f_0 = 0.5 \times 10^{-4}$ s^{-1} so as to approximate the latitude of the southern Californian shelf. Here we adopt the β-plane approximation $f = f_0 - \beta[y - L_c]$, where $\beta = 1.6 \times 10^{-1}$ (m s)$^{-1}$, $L_c = 2000$ km, and the value $f_0 = -10^{-4}$ s^{-1} is chosen to reflect the higher latitude of the eastern bight.

With all other parameters unchanged, the model was run for 60 days and the circulation over the shelf was found to be almost identical to that obtained for the basic f-plane case. The reason for this would appear to involve the slow phase speed of the internal Rossby waves that are important for the adjustment of the circulation. Anderson and Gill (1975) derived a timescale for this adjustment to be
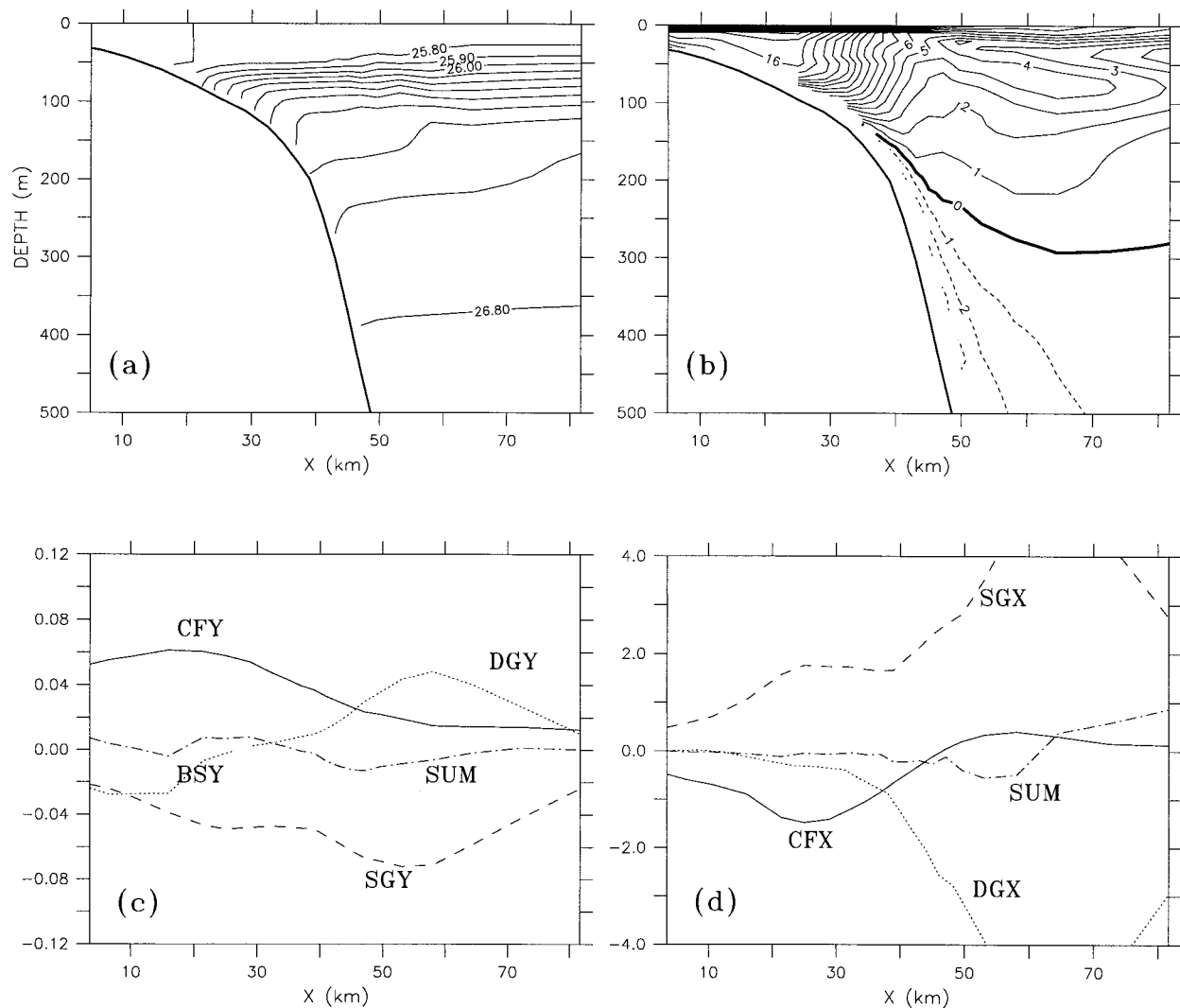
FIG. 13. Results obtained at section 2 and day 30 with the positive wind stress curl (11). (a) The density field σ_t: units kg m^{-3}, interval 0.1 kg m^{-3}. (b) The alongshore velocity field v. The solid (dashed) contours indicate flow to the east (west): units cm s^{-1}, interval 1 cm s^{-1}. (c), (d) Results for the alongshelf and cross-shelf integrated momentum equations. The labels are described in Fig. 10.

$$T_\beta = 4r_i/c_R = 4/\beta r_i, \tag{12}$$

where r_i and $c_R = \beta r_i^2$ are the internal deformation radius and Rossby wave speed. The scale (12) gives the time it takes for an internal Rossby wave to travel four internal deformation radii away from the shelf. Here, r_i is in the range (5–10) km so that $c_R = (0.4–1.6) \times 10^{-3}$ m s^{-1}. The scale $T_\beta = (290–580)$ days is larger than the integration time of 60 days, and much larger than the 180 day seasonal scale of winds within the bight. Rossby wave dispersion may not be important for this region.

Suginohara and Kitamura (1984) on the other hand considered upwelling closer to the equator and chose $f_0 = 0.5 \times 10^{-4}$ s^{-1} and $\beta = 2 \times 10^{-11}$ (m s)$^{-1}$ leading to a larger deformation radius $r_i = 24$ km, faster phase speed $c_R = 1.2 \times 10^{-2}$ m s^{-1}, and shorter adjustment time, $T_\beta = 96$ days. Certainly their results (Figs. 6 and 10) indicate phase speeds of order 10^{-2} m s^{-1} and that dispersion is important after a 100 days or so.

6. Summary and discussion

Using the Princeton Ocean Model, a study has been made of wind-forced downwelling slope currents on a zonal shelf and f plane. In agreement with the upwelling study of Suginohara (1982), the evolution of the current system over the first 10–20 days was characterized by a linear CTW phase and, notably, by the propagation of the first mode. In particular, before the arrival of this mode the downwelling was two-dimensional in nature, and almost all of the wind-driven Ekman flux was redirected offshore at depth. After the arrival of the first
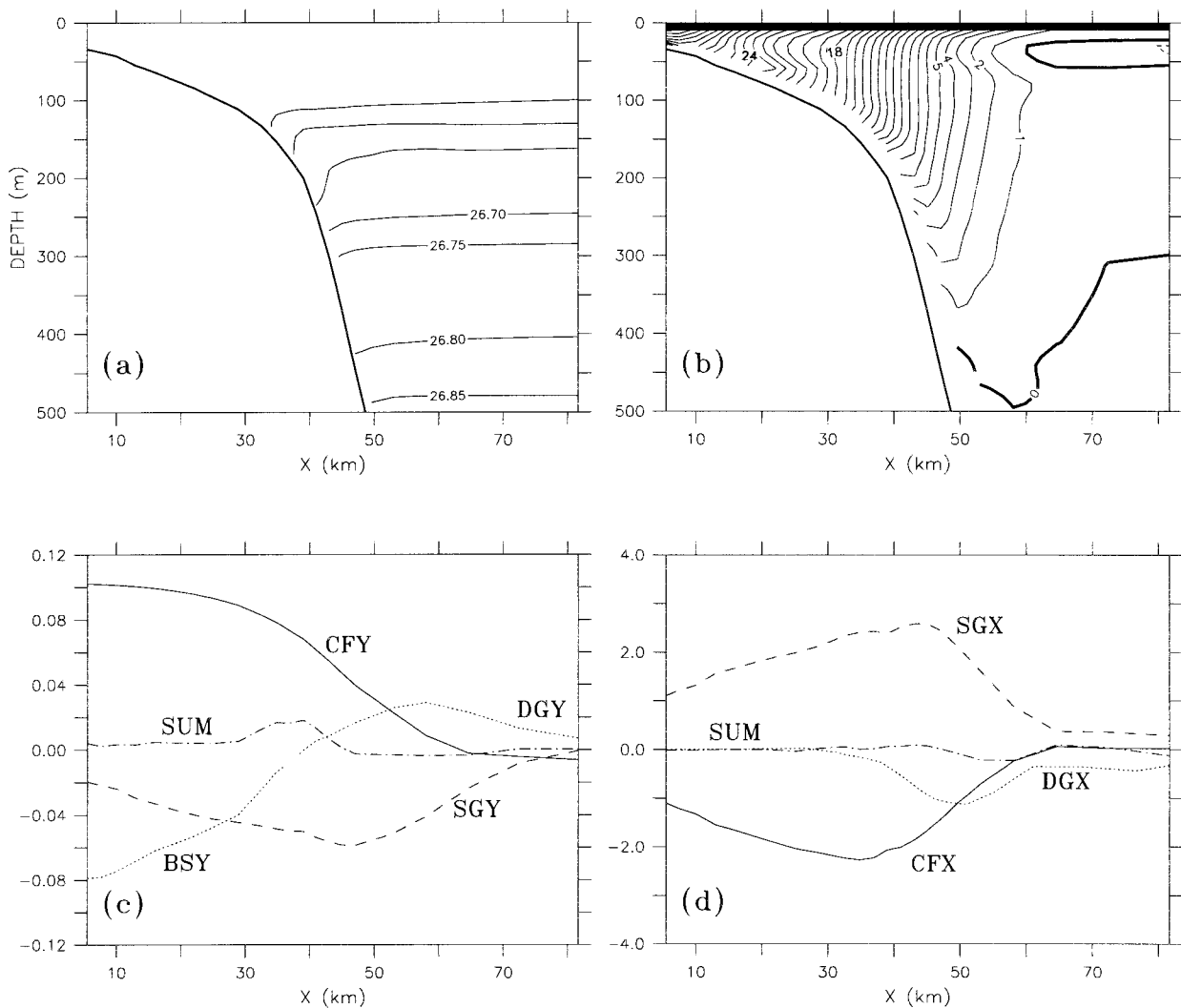
FIG. 14. Results obtained at section 2 and day 30 with a wintertime stratification. (a) The density field σ_t: units kg m^{-3}, interval 0.05 kg m^{-3}. (b) The alongshore velocity field v. The solid (dashed) contours indicate flow to the east (west): units cm s^{-1}, interval 1 cm s^{-1}. (c), (d) Results for the alongshelf and cross-shelf integrated momentum equations. The labels are described in Fig. 10.

mode, a divergence of the alongshore transport was set up and fed largely by the onshore Ekman transport due to the wind.

After this initial CTW phase, the dynamics of downwelling and upwelling systems appear to be quite different. Suginohara and Kitamura (1984) report that the upwelling system is insensitive to the presence or absence of bottom drag. They also claim that the long time (0–160 day) evolution of the upwelled system is accounted for by CTW dynamics and find that the UC ultimately disappears on an f plane.

None of these conclusions appear valid for the downwelling case here since the dynamics after 10 days or so are primarily governed by a BML phase. During this phase the depth of the downwelled BML grows and thermal-wind shutdown occurs. Indeed, within the forc-

ing region, the thermal wind shear associated with the BML was shown to account for up to 75% of the depth-integrated total and to be important in determining the magnitude of the UC. The shutdown of bottom stress over the slope was also shown to be important for the detachment of flow and spreading of isopycnals near the shelf break. Such spreading leads to an increase in the thermal wind and magnitude of the UC.

Thus, rather than disappearing, the UC grew in amplitude, reaching speeds of more than 10 cm s^{-1} or about one third of the CC. For the basic case considered, the alongshore transport associated with the UC was found to grow linearly with time to a value of about 0.7 Sv at day 60. A simple mass budget showed the UC to be largely fed and drained by on- and offshore transports of similar magnitude at the eastern and western ends of
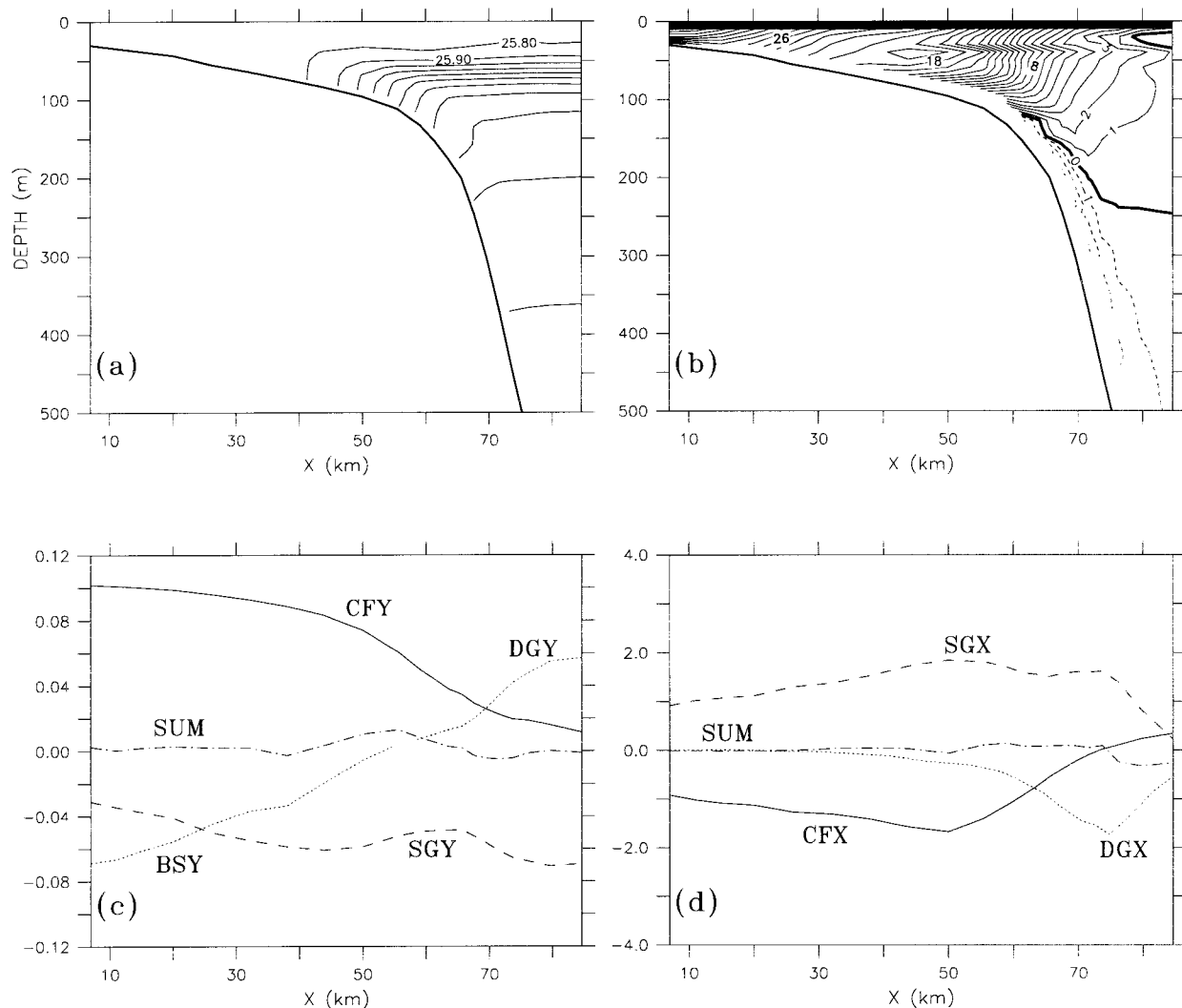
FIG. 15. Results obtained at section 2 and day 30 with a 25 km wider shelf and the original summertime stratification. (a) The density field σ_t: units kg m^{-3}, interval 0.1 kg m^{-3}. (b) The alongshore velocity field v. The solid (dashed) contours indicate flow to the east (west): units cm s^{-1}, interval 1 cm s^{-1}. (c), (d) Results for the alongshelf and cross-shelf integrated momentum equations. The labels are described in Fig. 10.

the forcing region. The transport of water upwelled into the overlying CC was found to be relatively small indicating only a weak connection between the water masses that are advected by the UC and CC.

While bottom stress is shut down over the slope, we do not find the results to be insensitive to the presence or absence of bottom drag. Results obtained without bottom drag showed an increase in the magnitude and divergence of the CC. The larger divergence in turn leads to a reduction in the interior cross-shelf transport, downwelling, and UC.

The downwelling solutions thus differ markedly from the upwelling results obtained by Suginohara and Kitamura (1984), and by simply reversing the sign of the wind stress, we obtain results that are similar to these authors: downwelling, rather than upwelling, is found

within the thermocline and over the slope and the UC is weak or nonexistent over the first 30 days or so. Thermal wind shear within the thin upwelled BML plays only a minor role in the formation of the UC and we plan to report on these results in the near future (Middleton 1999).

For the downwelling solutions obtained here, two conditions were found to be necessary for the existence of the UC. The first is that, since the UC is essentially geostrophic, the thermal wind shear must be large enough to overcome the opposing cross-shelf gradient in sea level. The second condition is that an alongshore pressure gradient in sea level must exist. The alongshore pressure gradient due to density $-p'_y/\rho_0$ and the Coriolis force $-fu$ generally act to decelerate the UC.

These results are perhaps not new, although the proof

of the second condition is novel and the results differ somewhat from those given by McCreary (1981) who obtained steady solutions adjacent to a vertical coastal wall. For these steady solutions, an UC was obtained, although vertical mixing of momentum was needed to balance the alongshore pressure gradient at the wall. For the solutions here, a steady state is not obtained (even after 60 days) and frictional effects and the vertical diffusivity is are generally zero in the interior and within the BML (following shutdown).

The effects of a β plane and of varying the stratification, shelf width, and wind stress were also investigated with the wintertime slope circulation of the Great Australian Bight in mind. Results suggest that Rossby wave dispersion may be unimportant in determining the slope circulation for the region since the adjustment time scale for the bight region (290–580 days) is larger than the seasonal scale of the winds (180 days).

Analyses by Trenberth et al. (1989) indicate a mean eastward stress within the bight of about 0.1 Pa. The stress increases to the south and the associated curl, 1.5×10^{-7} Pa m^{-1}, is an order of magnitude smaller than that used in the numerical solutions (10^{-6} Pa m^{-1}). The net Ekman displacement after 180 days would only be about 15 m, suggesting that the wind stress curl over the shelf may not be important.

The effects of a wind stress curl are of interest since the dynamics is different to the basic case above. Over the shelf slope, the Ekman pumping leads to a general upward and downward tilt of sea level and isopycnals leading to a broader CC and UC. In the basic (curl free) case, the UC was narrower since the thermal wind shear was larger near the shelf due to the BML and spreading of isopycnals.

During the autumn and winter months, the shelf stratification within the bight varies considerably and will act to modify the idealized slope circulation modeled here. In the western, central, and South Australian regions, the influx and formation of light water should act to provide a local thermocline over the shelf. In the far west however, the wind-forced circulation is likely to be dominated by the Leeuwin Current (Church et al. 1989), while in the central region where the shelf width exceeds 200 km the results above suggest that the wind-forced circulation may lie shoreward of the shelf break.

Off the narrow South Australian shelf, light water is present during the winter months (Godfrey et al. 1986) and zonal wind forcing may lead to an UC similar to that modeled here for the basic summertime case. Downwelling is found during May and, over the shelf, the currents are poleward (25 cm s^{-1}) during winter (Schahinger 1987).

As noted in the introduction, the poleward Zeehan Current also exists during the winter months off the west Tasmanian shelf. Measurements by Lyne and Thresher (1994) indicate that it is largely subsurface, confined to the outer slope, and has average speeds of about 50 cm s^{-1}. Within the top 500 m of the water column, isotherms are downwelled by around 100 m and the thermal wind shear is sufficient to drive a UC over the slope.

The cause of the Zeehan Current is unknown. The local mean winds, while zonal, are directed predominantly across isobaths due to the meridional orientation of the shelf. Possibly the forcing region for the current lies farther to the northwest and off the South Australian shelf. The deeply downwelled isotherms off Tasmania may represent the poleward extension of the hydrography within the forcing region. Such a result was found here (Figs. 4c and 5c) and suggested to arise from the adjustment and mixing of along-isobath variations in density within the BML.

In summary, the wind-forced shelf circulation within the bight will be influenced by the significant variations that occur in stratification and shelf width. While idealized, the results here do illustrate some of the fundamental dynamics of downwelling slope currents and should be of use in comparative studies of upwelling and in future analyses of the slope circulation of the Great Australian Bight.

REFERENCES

Allen, J. S., and P. A. Newberger, 1996: Downwelling circulation on the Oregon continental shelf. Part I: Response to idealized forcing. *J. Phys. Oceanogr.,* **26,** 2011–2035.

Anderson, D. L. T., and A. E. Gill, 1975: Spin-up of a stratified ocean, with applications to upwelling. *Deep-Sea Res.,* **22,** 583–596.

Blumberg, A. F., and G. L. Mellor, 1987: A description of a three-dimensional coastal ocean circulation model. *Three-Dimensional Coastal Ocean Models,* N. S. Heaps, Ed., Coastal and Estuarine Series, Vol. 4, Amer. Geophys. Union, 1–16.

Brink, K. H., and D. C. Chapman, 1985: Programs for computing properties of coastal-trapped waves and wind-driven motions over the continental shelf and slope. Tech. Rep. 85-17, Woods Hole Oceanographic Institution, 98 pp. [Available from Woods Hole Oceanographic Institution, Woods Hole, MA 02543.]

Chapman, D. C., and S. J. Lentz, 1997: Adjustment of stratified flow over a sloping bottom. *J. Phys. Oceanogr.,* **27,** 340–356.

Church, J. A., G. R. Cresswell, and J. S. Godfrey, 1989: The Leeuwin Current. *Poleward Flows Along Eastern Ocean Boundaries,* S. J. Neshyba, C. N. K. Mooers, and R. L. Smith, Eds., Coastal and Estuarine Studies, Vol. 34, Amer Geophys. Union, 230–254.

Clarke, A. J., 1977: Observational and numerical evidence for wind-forced coastal trapped long waves. *J. Phys. Oceanogr.,* **7,** 231–247.

Courant, R., K. Friedrichs, and H. Lewy, 1967: On the partial difference equations of mathematical physics. *IBM J. Res. Dev.,* **11,** 215–234.

Emanuel, K. A., 1994: *Atmospheric Convection.* Oxford University Press, 580 pp.

Garrett, C., P. MacCready, and P. Rhines, 1993: Boundary mixing and arrested Ekman layers. *Ann. Rev. Fluid Mech.,* **25,** 291–323.

Gawarkiewicz, G., and D. C. Chapman, 1991: Formation and maintenance of shelfbreak fronts in an unstratified flow. *J. Phys. Oceanogr.,* **21,** 1225–1239.

Godfrey, J. S., D. J. Vaudrey, and S. D. Hahn, 1986: Observations of the shelf-edge current south of Australia, winter 1982. *J. Phys. Oceanogr.,* **16,** 668–679.

Hickey, B., 1989: Poleward flow near the northern and southern boundaries of the U.S. west coast. *Poleward Flows Along Eastern Ocean Boundaries,* S. J. Neshyba, C. N. K. Mooers, and R. L. Smith, Eds. Coastal and Estuarine Studies. Vol. 34, Amer. Geophys. Union, 160–175.

Legeckis, R., and G. Cresswell, 1981: Satellite observations of sea-surface temperature fronts off the coast of western and southern Australia. *Deep-Sea Res.,* **28A,** 297–306.

Levitus, S., and T. P. Boyer, 1994: *World Ocean Atlas 1994 Temperature,* Vol. 4, *NOAA Atlas NESDIS.* U.S. Department of Commerce, Washington, D.C. 117 pp.

——, R. Burgett, and T. P. Boyer, 1994: *World Ocean Atlas 1994 Salinity,* Vol. 3: *NOAA Atlas NESDIS,* U.S. Department of Commerce, Washington, D.C. 99 pp.

Lyne, V. D., and R. E. Thresher, 1994: Dispersal and advection of *Macruronus novaezealandiae* (Gadiformes: Merlucciidae) larvae off Tasmania: Simulation of the effects of physical forcing on larval distribution. *Bio-Physics of Marine Larval Dispersal,* P. W. Sammarco and M. L. Heron, Eds., Coastal and Estuarine Studies, Vol. 45, Amer. Geophys. Union, 109–136.

MacCready, P., and P. B. Rhines, 1993: Slippery bottom boundary layers on a slope. *J. Phys. Oceanogr.,* **23,** 5–22.

McCreary, J. P., 1981: A linear stratified ocean model of the coastal undercurrent. *Philos. Trans. Roy. Soc. London A,* **302,** 385–413.

——, and S.-H. Chao, 1985: Three-dimensional shelf circulation along an eastern ocean boundary. *J. Mar. Res.,* **43,** 13–36.

——, Y. Fukamachi, and P. K. Kundu, 1991: A numerical investigation of jets and eddies near an eastern ocean boundary. *J. Geophys. Res.,* **96,** 2515–2534.

Mellor, G., 1986: Numerical simulation and analysis of the mean coastal circulation off California. *Contin. Shelf Res.,* **6,** 689–713.

Middleton, J. F., 1999: Wind-forced upwelling: The role of the surface mixed layer. *J. Phys. Oceanogr.,* in press.

——, and D. Ramsden, 1996: The evolution of the bottom boundary layer on the sloping continental shelf: A numerical study. *J. Geophys. Res.,* **101** (C8), 18 061–18 077.

Neshyba, S. J., C. N. K. Mooers, and R. L. Smith, Eds., 1989: *Poleward Flows along Eastern Ocean Boundaries.* Coastal and Estuarine Studies, Vol. 34, Amer. Geophys. Union, 374 pp.

Rochford, D. J., 1986: Seasonal Changes in the Distribution of Leeuwin Current Waters off Southern Australia. *Aust. J. Mar. Freshwater Res.,* **37,** 1–10.

Schahinger, R. B., 1987: Structure of coastal upwelling events observed off the south-east coast of South Australia during February 1983–April 1984. *Aust. J. Mar. Freshwater Res.,* **38,** 439–459.

Suginohara, N., 1982: Coastal upwelling: Onshore–offshore circulation, equatorward coastal jet and poleward undercurrent over a continental shelf-slope. *J. Phys. Oceanogr.,* **12,** 272–284.

——, and Y. Kitamura, 1984: Long term coastal upwelling over a continental shelf-slope. *J. Phys. Oceanogr.,* **14,** 1095–1104.

Trenberth, K. E., J. C. Olson, and W. G. Large, 1989: A global ocean wind stress climatology based on ECMWF analyses. Tech. Rep. NCAR/TN-338+STR, National Center for Atmospheric Research, Boulder, Colorado, 98 pp.